# In-situ synthesis of TiC/Ti composite coating by high frequency induction cladding

Yu, H.L.; Zhang, W; Wang, H.M.; Ji, X.C.; Song, Z.Y.; Li, Xiaoying; Lu, B.S.

*DOI:*
10.1016/j.jallcom.2017.01.084



*Document Version*
Peer reviewed version

*Citation for published version (Harvard):*
Yu, HL, Zhang, W, Wang, HM, Ji, XC, Song, ZY, Li, X & Lu, BS 2017, 'In-situ synthesis of TiC/Ti composite coating by high frequency induction cladding', *Journal of Alloys and Compounds*, vol. 701, pp. 244-255. https://doi.org/10.1016/j.jallcom.2017.01.084

# Accepted Manuscript


In-situ synthesis of TiC/Ti composite coating by high frequency induction cladding

H.L. Yu, W. Zhang, H.M. Wang, X.C. Ji, Z.Y. Song, X.Y. Li, B.S. Xu

PII: S0925-8388(17)30104-4

DOI: 10.1016/j.jallcom.2017.01.084

Reference: JALCOM 40451

To appear in: *Journal of Alloys and Compounds*

Received Date: 5 May 2016

Revised Date: 31 December 2016

Accepted Date: 8 January 2017

Please cite this article as: H.L. Yu, W. Zhang, H.M. Wang, X.C. Ji, Z.Y. Song, X.Y. Li, B.S. Xu, In-situ synthesis of TiC/Ti composite coating by high frequency induction cladding, *Journal of Alloys and Compounds* (2017), doi: 10.1016/j.jallcom.2017.01.084.

# In-situ synthesis of TiC/Ti composite coating by high frequency induction cladding

H.L. Yu[a*], W. Zhang[a], H.M. Wang[a], X.C. Ji[a,b], Z.Y. Song[a], X.Y. Li[b], B.S. Xu[a]

a. National Key Laboratory for Remanufacturing, Academy of Armored Forces Engineering, Beijing 100072, China;

b. School of Metallurgy and Materials, University of Birmingham, Birmingham B15 2TT, UK

[*]Corresponding author. Tel.: +86 10 66718580; fax: +86 10 66719325.

E-mail address: helong.yu@163.com (H.L. Yu).

Abstract:

The in-situ formation of TiC/Ti composite coating was achieved by induction cladding (IC) approach. The powder mixture of 70at% Ti and 30at% graphite were preplaced on a Ti6Al4V substrate and irradiated with a high frequency induction heating coil in Ar atmosphere. The cladded coating exhibited a practically dense and pore-free microstructure with metallurgical adherence to the substrate. Fine titanium carbides (TiC) were uniformly formed in the coating, which were confirmed by X-ray diffraction (XRD), X-ray photoelectron spectroscopy (XPS) and transmission electron microscope (TEM) analysis. Two temperature peaks within the coating indicates the induction cladding process is different from the point heating sources. Dissolution-precipitation mechanism is used to explain the formation of the composite coating and the in situ synthesis of the TiC particle reinforcements. The nanoindentation hardness of the TiC particles is about 22 GPa, which makes the microhardness of the composite coating (600 $HV_{0.2}$) nearly twice the microhardness of the Ti6Al4V substrate (340 $HV_{0.2}$). The hardness evolution of the composite coating is evaluated by the rule of mixtures and the predicted results are consistence with the measured ones.

Keywords: induction cladding, titanium matrix composites, composite coating, in-situ synthesis, TiC

## 1 Introduction

Titanium and its alloys are widely used in aerospace, marine, chemical and biomedical fields because of their desirable properties, such as low density, high specific strength, non-magnetism, biocompatibility, corrosion resistance, and good oxidation resistance [1–3]. However, low hardness and modulus, poor wear resistance and high friction coefficient limit their applications, especially to the fields where specific surface performances are required [4–6]. Wear is essentially a surface-dependent property that may be improved by appropriate modification of the surface microstructures and compositions without affecting the properties of the bulk materials [7, 8]. Titanium matrix composites (TMCs) have considerable potential, particularly for wear resistance applications because of their high hardness, high strength, high elastic modulus, and excellent high temperature stability. It is an effective solution to improve the surface properties by the particulate-reinforced titanium based composite coatings [9, 10]. The in-situ synthesis technology is a promising approach to fabricate the particulate-reinforced metal based composite coatings with elevated mechanical properties by the in-situ formed hard phases, which can improve the hardness, thermal stability, adherence of the coatings [11, 12]. Advanced composite coatings for titanium and its alloys with the in-situ particle reinforced structures have been rigorously investigated in the past decade, and it remains an active area of interdisciplinary researches.

Laser [13, 14], TIG [15] and plasma transferred arc [16] are commonly used for the in-situ deposition of the particle reinforced composite coatings. Among these methods, laser surface processing was regarded as the most promising solution [17]. Yang et al. [18] in-situ synthesized TiCN/TiN composite coating by laser cladding the mixture of Ti and C powder on Ti-6Al-4V substrate using nitrogen as protective gas. The in-situ deposited TiCN/TiN composite coating shows a remarkable improvement of microhardness (3–4 times) and wear resistance (10–11 times) compared to the Ti6Al4V substrate. Das et al. [19] in-situ synthesized TiB/TiN reinforced Ti6Al4V alloy composite coatings on Ti substrate by laser alloying from the premixed Ti6Al4V and BN powders. It showed that the hardness and Young's modulus of the composite coatings are positive correlated with the percentage of the BN powders. Li et al. [20] in-situ synthesized

the (TiC+TiB)/Ti composite coating on Ti6Al4V substrate by laser cladding from the preplaced Ti and $B_4C$ powders. The coating exhibited excellent wear resistance under dry sliding wear tests.

TiC is regarded as one of the best reinforcements in a titanium matrix due to its outstanding characteristics, such as high elastic modulus, similar density to Ti alloys, high melting point (3067 ℃), high hardness (2800 HV), good thermal stability, excellent wear resistance, high oxidation resistance and low friction coefficient [21, 22]. The in-situ TiC particles formed via the chemical reaction between Ti matrix and different carbon sources during the fabrication process can ensure that the Ti/TiC interfaces are clean and have strong metallurgical bonding [23]. In-situ Ti/TiC metal matrix composites have been fabricated using several techniques and the coatings exhibit excellent properties [16, 24, 25]. Zhang et al. [26] prepared a TiC reinforced composite coating on Ti6Al4V by laser induced melting and reaction of a powder mixture, which was consisted of Ti and $Cr_2C_3$ powders. It was found that the microstructures of the composite coating were related with the composition of the powder mixtures and the processing conditions. Savalani et al. [27] in-situ synthesized the TiC/Ti composite coating by laser cladding from the preplaced mixture of Ti powder and 20 wt% carbon nanotubes. The composite layers exhibited high hardness of 1125 $HV_{0.5}$ and excellent wear resistance due to the TiC reinforcements. According to the report [28] of Li, the in-situ TiC composite coatings fabricated with proper addition of CNT give promising high temperature wear resistance which is ten times higher than that of the titanium substrate. The improvement of the wear resistance is believed to be attributed to the reinforcement phase of TiC.

Induction heating has been used for heat treatment for decades. This process is time and energy saving, low cost, high reliability, fast thermal response, and low environmental hazards [29]. In recent years, it has been applied for the deposition and treatment of advanced coatings. Its applications involve laser-induction hybrid cladding of Ni based alloy [30], induction melting of Co based coating [31] and induction sintering of powder coatings [32]. Particularly, induction melting has received attention to prepare in situ metal matrix composite coatings on steel substrate. Wang et al. [33] in-situ synthesized TiC particle reinforced Ni-based alloy

composite coating by induction cladding from the mixture of nickel based alloy powders, titanium powders and graphite powders. The results indicate that the formation of the TiC particles increases with increasing of percentage of the titanium and graphite powders. The microhardness showed a gradually increasing trend within the composite coating, and the average microhardness of the composite coating is 1200 $HV_{0.2}$ which is 5 times that of the 16Mn steel substrate.

However, few studies have focused on in-situ synthesis of TMCs on Ti or its alloys by induction cladding method. Considering the induction heating method provides larger heating area compare to that of the point heating sources, such as laser, plasma, TIG, and electron beam, the induction cladding method can improve the efficiency of the deposition and reduce the defects (cracks and pores) within the coating due to the fast heating process. The aim of this study is to prove the feasibility of in-situ synthesized TMCs on Ti alloy surface by induction cladding. The phase composition, microstructure, micro-hardness, nanoindentation behavior and formation mechanism of the in-situ composite layer were investigated.

## 2 Experimental procedures

### *2.1. Raw materials and induction cladding process*

Ti6Al4V specimen with a size of 50 mm × 30 mm × 10 mm were used as substrates. The substrates were sandblasted and ultrasonic cleaned with acetone before the induction cladding. Ti powder (particle size 10–25 μm, purity 99.9%) and graphite powder (particle size 5–50 μm, purity 99.99%) were used as raw materials. The powder mixture was weighed to give a composition of 70at% Ti and 30at% C. This was blended in a three-dimensional mixing machine at a speed of 60 rpm for 24 h to make t hem homogeneous. Fig.1 shows the SEM image of the mixed raw powder. The homogenized powder was mixed by the binder (25wt% rosin, 75wt% turpentine) to form a slurry material and then preplaced on the cleaned substrate surface to form a layer of 2.0 mm thickness.

The induction cladding process is shown in Fig.2. The oscillation frequency of the induction heating equipment was 80–200 kHz with a maximum power output of 40 kW. The cladding processes were carried out using a flat induction coil with a size of 30 mm × 50 mm × 8 mm,

and the size of the square copper tube was 8.0 mm × 8.0 mm with a wall of 0.5 mm in thickness. The induction cladding was carried out using the following optimized processing parameters: The scanning rate of coil (v) was 1.5 mm/s, output power (P) was 15 kW, and distance between the coil and preset coating surface (a) was 5 mm.

*2.2. Characterization*

X-ray diffraction (XRD) with Cu Kα radiation (Bruker D8 Advance XRD) was used to identify the phase composition of the cladded coating and the raw powder mixture. After the cutting, hot mounting and cross-section grinding, and polishing, the polished coating cross-section was etched in the Kroll reagent (2vol%HF + 5vol%$HNO_3$ + 93vol%$H_2O$ solution). The morphologies and microstructures of the powders and the coatings were characterized using a field emission scanning electron microscopy (FESEM, FEI Nova NanoSEM 450) equipped with an energy dispersive X-ray spectroscope (EDS). Transmission electron microscope (TEM, Oxford JEOL 2100 LaB6) coupled with EDS was utilized to investigate the composite coating. The observations were carried out with an acceleration voltage of 200 kV. X-ray photoelectron spectroscopy (Thermo Fisher ESCALAB 250Xi with Al Kα X-ray source) was used to characterize the chemical states of cross-section of the in-situ TiC/Ti composite coating. High resolution peaks of Ti2p and C1s were recorded. The polished cross-section of the composite coating was etched by $Ar^+$ at 2 kV for 600 s before the XPS measurement.

Cross-section Vickers hardness of the composite coating were measured by a Buehler micromet 6030 tester. The measurements were performed at a load of 200 g and a dwelling time of 10 s. A fully calibrated Agilent Nano Indenter G200 nanoindentation tester was employed to measure the mechanical properties of the in-situ formed reinforced phase and the matrix of the composite coating, and the Ti6Al4V substrate. Continuous stiffness measurement (CSM) nanoindentation was carried out to determine the variation of indentation hardness ($H_{IT}$) and elastic modulus ($E_{IT}$) with indentation depth from 0 nm to 1000 nm. All indentations were done on the cross-section of the coating at a constant strain rate of 0.02 $s^{-1}$. The precise indent positions were preselected by using the integrated optical microscope equipped on the tester. To avoid the interaction between two adjacent indentations, the distance between any two test

points was larger than 50 μm. As the desired displacement or load reached the nano-indenter tip was held in position permitting creep effects to occur, and during the unloading part of the experiment a correction of thermal drifts was performed. Ten measurements were performed at each of the selected phase or material to increase the statistical reliability of the results. The CSM indentation method makes it possible to obtain indentation hardness ($H_{IT}$) and elastic modulus ($E_{IT}$) of materials from surface to certain depth by continuously recording the force and indentation depth during indenting materials surface. The indentation deformation behaviors were observed by a laser confocal microscope (LCM, Olympus OLS 4000). The area fraction of the reinforcing phase was calculated by image analysis, with the measured fractions for five optical micrographs from different portions of the upper-to-middle area and interface of the composite coating averaged. The measurements were made using Image-Pro Plus software.

**3 Results**

In-situ formed carbides were confirmed by both XRD and XPS analyses. Fig.3 shows the XRD patterns of the induction cladding composite coating and the preplaced Ti/graphite raw powder coating before cladding. The preplaced raw powder chiefly composed by α-Ti and graphite. After induction cladding, neither the peaks of the graphite nor the oxides of titanium were detected from the cladded composite coating, indicating that graphite has fully reacted. Diffraction peaks from the composite coating can well match the TiC phase. Furthermore, except the original α-Ti phase, a weak peak also can match the β-Ti phase due to the phase transition caused by the induction heating during cladding.

Fig. 4(a) and (b) show the Ti2p spectra and C1s spectra of the TiC/Ti composite coating, respectively. Peak at 454.3 eV was observed which corresponded to the Ti2p3/2 from the titanium carbide. Peak at 460.3 eV corresponds to Ti 2p2/1 from the titanium carbide [34, 35]. Fig. 4(b) shows the C 1s spectra of the composite coating. The C 1s peak of TiC is observed at 281.9 eV. The peak of graphite is absent in the spectrum. Peak at 285.3 eV is corresponding to carbon contamination [34].

The microstructures on the cross-section of the in-situ TiC/Ti composite coating were presented in Fig.5. It shows that the coating is dense and has a thickness of about 1.8 mm (see

Fig.5 (a)). The coating is well bonded to the Ti6Al4V substrate, and no interlayer cracks, gross defects are observed, such as porosity or lack of fusion. It indicates that the preplaced powders were fully melted during induction cladding. Moreover, dispersed phases with different size and shape are found in the different zones of the coating. TiC particles formed in the coating have two shapes, one is the near-sphere structure with a diameter of 1–3 μm (see inset image Fig.5 (b)); another is the needle like structure with a length of 5–10 μm and a diameter of 1–2 μm (see inset image Fig.5 (c)). It is verified by the analysis from EDS. It is shown in Fig.5 (b) and (c) that TiC particles not only segregated at Ti grain boundaries but also precipitated within a portion of Ti grains. The near-sphere particles are dispersed both at the boundaries and in the grains, while the needle-like particles are mainly dispersed at the boundaries. The in-situ formed TiC particles were uniformly distributed within the coating in micron scale, but the near-sphere particles were only formed in some Ti grains.

It can be seen in Fig.5 (d) that the surface of the composite coating is more flat compare to other in-situ composite coatings deposited by spot energy sources, such as laser [36], PTA [37] or GTAW [38]. This difference is mainly caused by the heat sources. Compared with the spot energy sources, high frequency induction heating coil can provide more energy and larger area of the preplaced powder coating could be irradiated, which leads to a large molten pool and a corresponding smooth surface after solidifying. In the present work, the coil (50 mm in width) scanned along the length direction of the specimen (30 mm in width), and the powder coating was melted within one scanning process. Surface roughness of the composite coating was measured in a range between 1.5 to 2.5 μm. Which means less machining allowance is needed and more materials are saved in practical application. Furthermore, the inset optical microscope (OM) image in Fig.5 (c) shows that the Ti matrix has a typical characteristic of bimodal structure, which consists of two typical structures: (1) a small amount of the primary equiaxed α-Ti phase and (2) large quantity of the platelet secondary α-Ti phase that separated by interface layer of the β-Ti (that is the structure of β transformation). The generation of β transformation was mainly caused by the induction heating, and β-Ti between platelet secondary α-Ti phases was also detected by XRD. Besides, a transition zone about 200 μm was formed between the

composite coating and the substrate, and no cracks or pores are observed, which indicates metallurgical bonds were produced between the coating and the substrate. The needle-like TiC particles are distributed in this transition zone (see Fig.5 (e)).

TEM characterizations were carried out to study the microstructures of the in situ formed spherical and needlelike TiC phases (see Fig.5 (b) and (c)), and Ti matrix (see Fig.5 (c)). Fig.6 shows the bright field TEM images and the corresponding SAD patterns of different phases within the TiC/Ti composite coating. Based on the analysis of the diffraction patterns, Fig.6 (a), (b) and (d) are corresponding to the TiC reinforcement with a cubic (NaCl) structure in the [001] beam direction. Thus, it was confirmed that needle-like TiC and spherical TiC were formed by the in situ reaction between Ti and graphite. Fig.6 (c), (e) and (f) indicate that the light coloured strip Ti matrix phase has a close-packed hexagonal (hcp) structure in the [2-1-10] beam direction, and the deep coloured interlaminar matrix phase has a cubic face-centered (bcc) structure in the [-113] beam direction.

A cross-sectional microhardness profile of the composite coating is shown in Fig.7. It is clear that the coating has relatively uniform hardness (approximately 600$HV_{0.2}$) at the first 1500 µm of the coating from the surface. Then the hardness decreases gradually to approximately 440 $HV_{0.2}$ at the interface between the coating and the transition zone The hardness at the interface between the transition zone and the substrate is about 410 $HV_{0.2}$, which is still higher compare to the hardness of the Ti6Al4V (340 $HV_{0.2}$).

Nanoindentation tests were performed to investigate the mechanical properties of the phases in nano/micro scale. Typical 3D optical micrographs of the indented positions on different phases, at a maximum indenter depth of 1000 nm, are reported in Fig.8 (a)–(d). Triangular pyramid craters can be formed when the indentation tip penetrates in different phases. The indentation hardness ($H_{IT}$) and indentation modulus ($E_{IT}$) can be obtained by continuously recording the force and indentation depth during indenting materials surface.

Fig.9 (a), (b) and (c) show the load-displacement curve, $H_{IT}$ profile and $E_{IT}$ profile, respectively. Compare to substrate and other phases, higher indentation load is needed to make the indentation depth to 720 nm for TiC phase, which means that the TiC phase possesses a

relatively high hardness. The load-depth curves of the substrate and the equiaxed α-Ti phase have similar trends. For deeper indentation depth from 720nm to the final maximum, the indentation load for the β transformation is the highest. Furthermore, it is noted that the maximum indentation loads for the TiC phase and the equiaxed α-Ti rich phase are similar, indicating they have similar average hardness. The results of indentation hardness and modulus were consistent with the load-depth observations. The $H_{IT}$ profile of TiC phase increases with the indentation depth in the range from 0 nm to about 70 nm, stabilizes from 70 nm to 120 nm, and then decreases. The other profiles of hardness have the same trends: increase rapidly in the depth range from 0 nm to 40 nm, and stabilize when indented deeper than 40 nm. For the variation of modulus, the situation is similar with the hardness for all the tested samples. The in situ TiC phase and the structure of β transformation exhibit a peak hardness of 22 GPa and an average hardness of 6.1 GPa, and a peak modulus of 280 GPa and an average modulus of 200 GPa, respectively. The equiaxed α-Ti rich phase and the substrate possessed the similar property: an average hardness of 4 GPa, and a modulus of 150 GPa.

## 4. Discussions

### *4.1 Forming mechanism of the induction cladding coating*

It is well known that the current distribution is not uniform when an alternating current flows through a conductor. The maximum value of the current density will be located on the surface of the conductor, and it decreases from the conductor surface toward its center. The phenomenon of nonuniform current distribution within the conductor cross-section is called the skin effect, which is one of the major factors that cause the concentration of eddy current in the surface layer of the workpiece during induction heating. Because of the skin effect, approximately 86% of the induction power will be concentrated in the surface layer. The temperature will therefore decrease from the surface of the preplaced coating toward the interface and the substrate during induction cladding. On the other hand, induction heating relies on two mechanisms of energy dissipation for the purpose of heating. These are energy losses due to Joule heating and energy losses associated with magnetic hysteresis [39]. The Joule heating is the sole mechanism of heat generation in nonmagnetic materials such as austenitic

stainless steels, and aluminum, titanium and their alloys. In this case, the heat by induced eddy currents in the workpiece is proportional to the square of the current intensity. It is obvious that the “dense” Ti6Al4V substrate has much less electrical resistance compared to the “loose” preplaced coating on the substrate. Therefore, the induction heating rate of coating/substrate interface is higher than that of the preplaced coating near interface, leading to a second temperature peak at the interface besides the coating surface.

To have a better understanding of the heating process and the forming mechanism of the induction cladding coating, less power was utilized to get a not fully reacted composite coating and its cross section images are shown in Fig.10. The coating surface and the interface regions are dense. TiC particles have similar morphologies with that shown in Fig.5, which can be clearly distinguished, indicating the preplaced Ti and graphite powders were melted completely at these regions even under less heating power. However, in the middle area of the coating, plenty of black particles covered by gray layer are observed. It is verified by EDS analysis that the particles are graphite and the layers are TiC phases. Large amount of residual graphite particles indicate that the melting of Ti powder was poor in this area, and the formation, dissolution, and precipitation processes for the formation of TiC were incomplete due to the relatively low temperature during induction cladding. It indicates that during the induction cladding, temperatures at the surface and the interface areas are higher than that in the middle zone. It proved the presence of two temperature peaks within the coating, one at the surface and the other at the interface. Hence, induction heating is different from the point heating sources, such as laser, plasma, electron beam, and oxyacetylene flame. The melting processes for these sources are from the surface to the center. In a induction melting process, the coating can be melted from the surface and the interface simultaneously by the joule heat derived from eddy current, which can provide a rapid melting process for the deposition of the coating. Especially the melting process happens at the interface, which can lead to metallurgical bonded interface between the coating and the substrate.

*4.2 Solidification process and in-situ forming mechanism of TiC*

During induction cladding, the reaction of Ti and graphite can be expressed as follows:

$$Ti + C \rightarrow TiC \quad (1)$$

The standard Gibbs free energy, $\Delta G_T$, and standard formation enthalpy, $\Delta H_T$, of the above reaction was calculated using thermodynamic data from Ye [40]. As shown in Fig. 11, the $\Delta G_T$ is negative up to 2500 K, indicating the reaction was feasible thermodynamically and TiC can be formed at this condition. Moreover, the $\Delta H_T$ is also negative, which indicates that the reaction is exothermic and can spontaneously occur. The XRD, XPS, TEM, and SEM analysis of the composite coating verified that the TiC particles were in situ synthesized from the preplaced coating consist Ti and graphite powders by induction cladding, leading to a significantly increase of the microhardness of the composite coating compared to the substrate.

The growth mechanism of TiC includes: (1) diffusion mechanism and (2) dissolution–precipitation mechanism. A study on the in-situ TiC/Al composite coating shows that the high temperature self-propagating reaction between Ti and C occurs below 1500 K [41]. Tong [42, 43] et al. reported that when the temperature is lower than 1554 K, the growth of TiC is dominated by the diffusion process. When it is higher than 1554 K, the TiC is formed by the dissolution–precipitation process. Generally, the diffusion mechanism happens when the synthesis temperature is lower than the liquidus temperature. When the synthesis temperature is higher than the liquidus temperature, the dissolution-precipitation processes happen, which includes three steps: I formation through in-situ reaction, II dissolution in a high-temperature melt, III nucleation and growth before solidification [42]. The dissolution-precipitation mechanism is applicable to the formation of the reinforcing phases of the composite materials such as TiC/Ti, TiB, and (TiC+TiB)/Ti obtained by the laser, plasma, electron beam, and induction methods.

The infrared temperature measurement shows that the highest surface temperature of the samples during the induction cladding was higher than 2300 K. Based on the Ti–C binary phase diagram [44] shown in Fig.12, the in-situ synthesized TiC particles will dissolve completely in the liquid Ti molten pool, and then precipitate. The TiC particles were first nucleated and then growth during the subsequent cooling and solidification. In this case, the in-situ formation of TiC/Ti composite coating by induction cladding can be explained as follows: the preplaced Ti powder transformed from α-Ti to β-Ti when temperature was higher than 1155 K, and then β-Ti

reacted with graphite and formed TiC. When the temperature was higher than 2000 K, β-Ti melted and formed the molten pool, in which the in-situ-formed TiC particles dissolved and precipitated during the cooling process. The sizes and morphologies of the TiC reinforcing phases were mainly influenced by the cooling rate during the solidification and the crystalline structure of the TiC.

The binary phase diagram of Ti–C shows that TiC precipitates from the liquid phase and then form the primary crystal of TiC during the solidification. As TiC has the B1 (NaCl style) crystal structure [45], the growth rate on the symmetric crystal faces was the same during the nucleation, favoring the formation of the symmetric structure, i.e., isometric spherical particles. Moreover, the surface energy for the formation of spherical particles is the lowest, and thus the nucleation was the easiest. Therefore, spherical TiC particles are primary formed during the cooling process. However, under the nonuniform cooling conditions, the growth rate along the undercooling direction will be faster. Observing the liquidus and solidus temperatures of L + TiC, the rise of the former was steeper, favoring the appearance of constitutional undercooling, and forming the dendrite due to the preferential growth along the undercooling direction. Moreover, temperatures rise up faster at the surface and the interface areas, which act as two heating sources for the synthesis process. The cooling rates at these two areas are also higher than that in the middle area when induction heating stopped, leading to the growth of the strip-type TiC phases as shown in Figs. 5(c) and 5(d). The cooling condition in the middle of the coating was relatively stable, resulting in the formation of the near-spherical TiC phases.

In the further cooling process, the β-Ti and TiC (binary eutectic) precipitated from the liquid phase when reaching the binary eutectic line of L→β-Ti + TiC, and the TiC was spherical. When approaching to the solid phase, the diffusion rate decreases, whereas the TiC nucleation rate increases, leading to the precipitation of smaller TiC crystals from the binary eutectic compared to the primary TiC phase. With a further decrease of the temperature, the reaction of β-Ti + TiC→ α-Ti occurred in the solid-phase area. Few solid phase reactions happen due to the low temperature and fast cooling rate.

*4.3 Reinforcement mechanism and mechanical behaviors of in-situ TiC*

The $H_{IT}$ and $E_{IT}$ of in-situ TiC phase are strongly affected by the indentation depth. This scale-dependent hardness behavior is related to the composite microstructure constructed by the hard reinforcements and the soft matrix, which is different from the well-known indentation size effect (ISE) [46] and related to strain gradients and geometrically necessary dislocations. As shown in [46] indeed, such effect will be dominant when the indentation depth is very small. The nanoindentation hardness is calculated by the ratio of the indentation load to the projection area of the plastic deformation of the sample [47]. At very small depth, only elastic deformation occurs. With the increase of indentation depth, plastic deformation occurs and causes a rapid increase of the indentation hardness at the depth of dozens of nanometers, and the measured values above that depth are generally considered to represent the real mechanical properties. Therefore, the rapidly increasing hardness and modulus at lower depth shown in Fig.9 (b) and (c) can be attributed to the indentation size effect. However, the ISE cannot explain the hardness behaviors for the in-situ TiC. But it is helpful to explain the hardness behaviors β transformation, equiaxed α-Ti rich phase and Ti6Al4V substrate, which do not possess a particle reinforced microstructure. Their hardness stabilizes rapidly at low depth. Therefore, the average hardness measured deeper than dozens of nanometers reflects the behavior of the structure of β transformation and the equiaxed α-Ti phase, and they exhibit the average hardness of 6.1 GPa and 4.0 GPa, respectively.

To clarify the mechanical behaviors of the in-situ formed TiC particles and understand the correlation between the indentation depth ($h$), the indentation volume and the size of the TiC particle, the size of residual nanoindentation impression is corresponding to the indentation displacements during the loading process. In general, the indentation radius, $R_i$, describes the distance between the center and the vertex of the equilateral triangle indentation mark, which can be used to calculate the volume of the indentation crater. For a standard Berkovich indenter, there is a relationship between $R_i$ and the indentation depth (h), which can be expressed as:

$$R_i = 2h \cdot \mathrm{tg}a_1 \tag{2}$$

where $a_1$ denotes the angle between a plane and the altitude of the triangular pyramid indentation marks (or the indenter), and in the present paper, for a diamond Berkovich indenter

the angle $a_1=a_2=a_3=65.3°$.

An indentation depth of 120 nm corresponds to an indentation radius of about 520 nm according to the above equation. At this depth, although the deformation volume is smaller than the size of a TiC particle in the cross-section of the composite coating, it approaches to 1/10 of the dimension of a single TiC particle in the direction vertical to the cross-section, because the size of the TiC particles (shown in Fig.8 (a)) were probably reduced from original 3-4 μm to about 1-2 μm during the grinding process. The indentation on the TiC particle, in this case, can be regarded as indenting on hard film with a soft substrate, and the influence of bottom soft Ti matrix increases with the increasing of the indentation depth, especially when the depth deeper than 1/10 thickness of the coating according to ISO 14577 standard [48]. Therefore the decreasing hardness of TiC phase, when the depth deeper than 120 nm, can be explained by the variation of the indented volume of bottom Ti matrix. In this case, the hardness measurements of the TiC phases were less influenced by the matrix phase of α-Ti and β-Ti. The in situ TiC phase exhibits an average hardness of 22 GPa in the depth range from 70 nm to 120 nm, the value corresponds with the hardness levels in the range of 2000-3000 HV reported by Jiang [49]. Whereas with the increasing of the indentation depth, more influences from the bottom and surrounding soft Ti matrix were achieved to lower the hardness. It is shown in Fig.9 (b) and (c) that obvious inflection points appear at the indentation depth of 450 nm in curves of TiC. In which the size of the indentation craters are close to the sizes of the TiC particles, and the hardness and the modulus will gradually decrease to that of the Ti matrix.

The Vickers hardness values of the in situ TiC particles and the matrix phases of α-Ti and β-Ti can be recalculated from the nanoindentation hardness according to the following formula [48]:

$$H_V = 94.5H_{IT} \quad (3)$$

where $H_V$ is the microhardness value by Vickers hardness method, HV, and $H_{IT}$ is the indentation hardness by nanoindentation method, GPa.

The recalculated hardness for the dispersed particles and the matrix of the composite coating are feasible for the estimating of the hardness as a function of the phase fractions according to a

Rule of Mixtures (ROM) calculation. The hardness of the in situ TiC/Ti composite coating can be calculated according to the models of Iso-Strain, Iso-Stress and Power-Law, associated with high, low and middle volume fractions of reinforced phase, respectively [24, 50, 51]:

$$H_{composite} = H_{TiC}f_{TiC} + H_{matrix}(1 - f_{TiC} \quad \text{(Iso-strain)} \tag{4}$$

$$H_{composite}^{-1} = H_{TiC}^{-1}f_{TiC} + H_{matrix}^{-1}(1 - f_{TiC}) \text{(Iso-stress)} \tag{5}$$

$$H_{composite} = H_{matrix}(\frac{H_{TiC}}{H_{matrix}})^{f_{TiC}} \qquad \text{(Power-Law)} \tag{6}$$

where $f_{TiC}$ and $f_{matrix}$ are the area fractions of the TiC particles and the matrix, respectively. $f_{TiC}$ + $f_{matrix}$ =1. $H_{composite}$, $H_{TiC}$, and $H_{matrix}$ are the hardness of the composite, TiC particles and the matrix, respectively.

These equations are applied for $f_{TiC}$ ranging from 0 to 1, using $H_{TiC}$ = 2079 HV (recalculated form $H_{IT}$ of 22GPa), and assuming that the matrix is entirely composed of structure of β transformation with $H_{matrix}$=567 HV (recalculated form $H_{IT}$ of 6.1 GPa) or equiaxed α-Ti rich phase with $H_{matrix}$ =378 HV (recalculated form $H_{IT}$ of 4.0 GPa), or the mixture of 75vol% structure of β transformation and 25vol% equiaxed α-Ti rich phase with $H_{matrix}$ =520 HV (calculated by Iso-strain model). The results of the predictions according to all three models are demonstrated in Fig.13. To examine the validity of these calculations, the predicted hardness values are also compared with the measured, near-constant, microhardness value at the upper-middle coating, where $f_{TiC}$ is estimated as 0.11, and $f_{TiC}$ at the interface, is 0.02.

The measured microhardness of the middle–upper coating (~600 $HV_{0.2}$) agrees well with the predicted results of the rule of mixtures (ROM). If the coating matrix was supposed to only contain the β transformation, the measured hardness of the coating was consistent with the Iso-stress model. When the equiaxed α-Ti phase was in dominant, the measured hardness of the coating was consistent with the predicted value obtained from the Iso-strain model. In the case when the coating was combined with 75vol% of β transformation and 25vol% of equiaxed α-Ti phase, the measured hardness of the coating was consistent with the predicted value obtained from the Power-Law model, which is consonant with the results obtained by Brian et al. [24]. The measured hardness in the interface area (~410 HV) was consistent with the predicted value from ROM with the assumption that the matrix of the interface was equiaxed α-Ti phase. About

2% of TiC reinforcements were formed in the interface area and its hardness is still dominant by the equiaxed α-Ti phase.

The abovementioned results indicate that the hardness of the composite coating reinforced by the in-situ synthesized TiC can be effectively predicted by using the ROM method. Appropriate hardness and the concentration of the matrix and reinforced phases should be carefully choosing. The in-situ TMCs coating can be designed with suitable structures to meet hardness requirements for the application, which includes the selection of the percentage of the matrix and the reinforcements.

**5 Conclusions**

The in-situ synthesized TiC particles reinforced Ti composite coating was successfully prepared by the high frequency induction cladding method on Ti6Al4V substrate. The composite coating has a flat surface and a dense structure without defects such as pores and cracks. Metallurgical bond was formed between the coating and the substrate. The formation of TiC particle undergoes in-situ reaction between Ti and C, dissolution in the high-temperature Ti melt, nucleation and growth before solidification. The in-situ deposited TiC phase has a hardness of 22 GPa and a modulus of 270 GPa. Two shapes of TiC particles were formed in the coating, near-sphere phase with a diameter of 1–5 μm, needle like phase with a length of 5–10 μm and a diameter of 1–2μm. Two temperature peaks were found within the coating during induction cladding, which leads to a rapid heating and solidification of the surface and the interface of the composite coating. That affects the morphology and distribution of the TiC particles, and results in a good metallurgical bonding between coating and substrate. The matrix was formed by the β transformation and the equiaxed α-Ti phase. A relatively uniform hardness in the range of 590–610 $HV_{0.2}$ is achieved at surface area of the coating. The hardness then decreases to 440–410 $HV_{0.2}$ at the interface, and the hardness of the substrate is 340 $HV_{0.2}$. The hardness evolution agrees well with the prediction of the Rule of Mixtures, which is related with the percentage of the reinforcements and the type of matrix.

**Acknowledgment**

The research was supported by the National Science and Technology Supporting Project of

China (2011BAF11B07, 2011BAC10B05), National Natural Science Foundation of China (51005243) and Natural Science Foundation of Beijing (3132024).

**References**

[1] Y.S. Tian, C.Z. Chen, S.T. Li, Q.H. Huo, Research progress on laser surface modification of titanium alloys, Appl. Surf. Sci. 242 (2005) 177–184.

[2] R. Boyer, An overview on the use of titanium in the aerospace industry, Mater. Sci. Eng. A 213 (1996) 103–114.

[3] W. Ho, T. Chiang, S. Wu, H. Hsu, Mechanical properties and deformation behavior of cast binary Ti–Cr alloys, J. Alloys Compd. 468 (2009) 533–538.

[4] B.G. Guo, J.S. Zhou, S.T. Zhang, H.D. Zhou, Y.P. Pu, J.M. Chen, Phase composition and tribological properties of Ti–Al coatings produced on pure Ti by laser cladding, Appl. Surf. Sci. 253 (2007) 9301–9310.

[5] J.N. Li, C.Z. Chen, T. Squartini, Q.S. He, A study on wear resistance and microcrack of the Ti3Al/TiAl + TiC ceramic layer deposited by laser cladding on Ti–6Al–4V alloy, Appl. Surf. Sci. 257 (2010) 1550–1555.

[6] Y. Wang, H.M. Wang, Wear resistance of laser clad $Ti_2Ni_3Si$ reinforced intermetallic composite coatings on titanium alloy, Appl. Surf. Sci. 229 (2004) 81–86.

[7] M. Hazra, A.K. Mondal, S. Kumar, C. Blawert, Narendra B. Dahotre, Laser surface cladding of MRI 153M magnesium alloy with ($Al+Al_2O_3$), Surf. Coat. Technol. 203 (2009) 2292–2299.

[8] J. Li, Z.S. Yu, H.P. Wang, M.P. Li, Microstructural evolution of titanium matrix composite coatings reinforced by in situ synthesized TiB and TiC by laser cladding, Inter. J. Miner. Metall. Mater. 17 (2010) 481–488.

[9] M. Kulka, N. Makuch, P. Dziarski, A. Piasecki, A. Miklaszewski, Microstructure and properties of laser-borided composite layers formed on commercially pure titanium, Opt. Laser Technol. 56 (2014) 409–424.

[10] G.J. Li, J. Li, X. Luo, Effects of post-heat treatment on microstructure and properties of laser cladded composite coatings on titanium alloy substrate, Opt. Laser Technol. 65 (2015)

66–75.

[11] Y. Wu, A.H. Wang, Z. Zhang, H.B. Xia, Y.N. Wang, Wear resistance of in situ synthesized titanium compound coatings produced by laser alloying technique, Surf. Coat. Technol. 258 (2014) 711–715.

[12] Q. Qi, Y. Liu, H. Zhang, J. Zhao, L.L. Gai, Y.H. Huang, Z.R. Huang, The formation mechanism of TiC particles in TiC/Ni composites fabricated by in situ reactive infiltration, J. Mater. Sci. 51 (2016) 7038–7045.

[13] M. Li, J. Huang, Y.Y. Zhu, Z.G. Li, Effect of heat input on the microstructure of in-situ synthesized TiN–TiB/Ti based composite coating by laser cladding. Surf. Coat. Technol. 206 (2012) 4021–4026.

[14] J.N. Li, C.Z. Chen, Q.S. He, Influence of Cu on microstructure and wear resistance of TiC/TiB/TiN reinforced composite coating fabricated by laser cladding, Mater. Chem. Physics 133 (2012) 741–745.

[15] R.J. Yang, Z.D. Liu, G. Yang, Y.T. Wang, Study of in-situ synthesis TiCp/Ti composite coating on alloy Ti6Al4V by TIG cladding, Procedia Eng. 36 ( 2012 ) 349–354.

[16] D.Q. Chen, D. Liu, Y.F. Liu, H.M. Wang, Z. Huang, Microstructure and fretting wear resistance of γ/TiC composite coating in situ fabricated by plasma transferred arc cladding, Surf. Coat. Technol. 239 (2014) 28–33.

[17] D.J. Liu, P.P. Hu, G.Q. Min. Interfacial reaction in cast WC particulate reinforced titanium metal matrix composites coating produced by laser processing, Opt. Laser Technol. 69 (2015) 180–186.

[18] Y.L. Yang, W.M. Yao, H.Z. Zhang, Phase constituents and mechanical properties of laser in-situ synthesized TiCN/TiN composite coating on Ti–6Al–4V. Surf. Coat. Technol. 205 (2010) 620–624.

[19] M. Das, V. K. Balla, D. Basu, I. Manna, T.S. Sampath Kumar, A. Bandyopadhyay. Laser processing of in situ synthesized TiB–TiN-reinforced Ti6Al4V alloy coatings. Scripta Materialia 66 (2012) 578–581.

[20] J. Li, Z.S. Yu, H.P. Wang, Wear behaviors of an (TiB+TiC)/Ti composite coating fabricated

on Ti6Al4V by laser cladding, Thin Solid Films 519 (2011) 4804–4808.

[21] H. Kawasaki, K. Doi, S. Hiraishi, Formation and properties of TiC thin films by pulsed Nd/YAG laser deposition, Thin Solid Films 374 (2000) 282–286.

[22] Z.Y. Ma, R.S. Mishra, S.C. Tjong, High-temperature creep behavior of TiC particulate reinforced Ti-6Al-4V alloy composite, Acta Mater. 50 (2002) 4293–4302.

[23] L.J. Huang, L. Geng, H.Y. Xu, H.X. Peng, In situ TiC particles reinforced Ti6Al4V matrix composite with a network reinforcement architecture, Mater. Sci. Eng. A 528 (2011) 2859–2862.

[24] Brian C. Langelier, Shahrzad Esmaeili, In-situ laser-fabrication and characterization of TiC-containing Ti–Co composite on pure Ti substrate, J. Alloys Compd. 482 (2009) 246–252.

[25] M.J. Hamedi, M.J. Torkamany, J. Sabbaghzadeh, Effect of pulsed laser parameters on in-situ TiC synthesis in laser surface treatment, Opt. Lasers Eng. 49 (2011) 557–563.

[26] S. Zhang, W.T. Wu, M.C. Wang, H.C. Man. In-situ synthesis and wear performance of TiC particle reinforced composite coating on alloy Ti6Al4V. Surf. Coat. Technol. 138 (2001) 195–100.

[27] M.M. Savalani, C.C. Ng, Q.H. Li, H.C. Man, In situ formation of titanium carbide using titanium and carbon-nanotube powders by laser cladding, Appl. Surf. Sci. 258 (2012) 3173–3177.

[28] Q.H. Li, M.M. Savalani, Q.M. Zhang, L. Huo, High temperature wear characteristics of TiC composite coatings formed by laser cladding with CNT additives, Surf. Coat. Technol. 239 (2014) 206–211.

[29] S. Zinn, S. L. Semiatin, Elements of induction heating, ASM International, 1988: 1–8.

[30] S.F. Zhou, X.Q. Dai, Microstructure evolution of Fe-based WC composite coating prepared by laser induction hybrid rapid cladding, Appl. Surf. Sci. 256 (2010) 7395–7399.

[31] J.H. Chang, J.M. Chou, R.I. Hsieh, J.L. Lee, Influence of fusing temperature on microstructure, wear and corrosion resistance of induction melted bimetal of Co-based alloy and AISI 4140 steel, Mater. Chem. Phys. 118 (2009) 314–321.

[32] Yu. N. Gafo, I. A. Sosnovskii, Thermal parameters for centrifugal induction sintering of powder coatings, Powder Metall. Met. Ceram. 48 (2009) 105–111.

[33] Z.T. Wang, Y.D. Wang, Microstructure and properties of in-situ synthesis of TiC particle reinforced composite coating by induction cladding. Key Eng. Mater. 336-338 (2007) 1725–1727.

[34] C.Y. Tang, C.T. Wong, L.N. Zhang, M.T. Choy, T.W. Chow, K.C. Chan, T.M. Yue, Q. Chen, In situ formation of Ti alloy/TiC porous composites by rapid microwave sintering of Ti6Al4V/MWCNTs powder, J. Alloys Compd. 557 (2013) 67–72.

[35] L.H. Zhang, R.V. Koka, A study on the oxidation and carbon diffusion of TiC in alumina–titanium carbide ceramics using XPS and Raman spectroscopy, Mater. Chem. Phys. 57 (1998) 23–32.

[36] X.B. Liu, X.J. Meng, H.Q. Liu, G.L. Shi, S.H. Wu, C.F. Sun, M.D. Wang, L.H. Qi, Development and characterization of laser clad high temperature self-lubricating wear resistant composite coatings on Ti–6Al–4V alloy, Mater. Des. 55 (2014) 404–409.

[37] D.L. Wu, X.B. Wang, Defects in the in situ synthesized $TiB_2$/Fe composite coatings during PTA process, Appl. Surf. Sci. 257 (2011) 10119–10125.

[38] W.Q. Yan, L. Dai, C.B. Gui, In situ synthesis and hardness of TiC/$Ti_5Si_3$ composites on Ti-5Al-2.5Sn substrates by gas tungsten arc welding, Inter. J. Miner. Metall. Mater. 20 (2013) 284–289.

[39] E. Rapoport, Y. Pleshivtseva, Optimal control of induction heating processes. Taylor and Francis Group, 2007:1–33.

[40] D.L. Ye, Practical inorganic thermodynamics manual, Metallurgical Industry Press, Beijing, 2002.

[41] T. Nukami, M.C. Flemings, In situ synthesis of TiC particulate-reinforced titanium matrix composites. Metall. Mater. Trans. 26A (1995) 1877–1884.

[42] X.C. Tong, H.S. Fang, Al-TiC composites in situ –processed by ingot metallurgy and rapid solidification technology: Part I. Mechanical behavior. Metall. Mater. Trans, 29A (1998) 875–891.

[43] X.C. Tong, H.S. Fang, Al-TiC composites in situ –processed by ingot metallurgy and rapid solidification technology: Part II. Mechanical behavior. Metall. Mater. Trans, 29A (1998) 893–902.

[44] H. Duschanek, P. Rogl, A critical assessment and thermodynamic calculation of the boron-carbon-titanium (B-C-Ti) ternary system, J. Phase Equilib. 16 (1995) 46–60.

[45] W. Jeitschko, R. Pottgen, R.D. Hoffman, Structural chemistry of hard materials. Handbook of ceramic hard materials, ed. R. Riedel. Wiley- VCH, New York, 2003:12–16.

[46] W.D. Nix, H. Gao, Indentation on size effects in crystalline materials: a law for strain gradient plasticity, J. Mech. Phys. Solids 46 (1998) 411–425.

[47] W.C. Oliver, G.M. Pharr, An improved technique for determining hardness and elastic modulus using load and displacement sensing indentation experiments, J. Mater. Res. 7 (6) (1992) 1546–1583.

[48] Metallic materials–Instrumented indentation test for hardness and material parameters, ISO 14577, 2002.

[49] C.C. Jiang, T. Goto, T. Hirai, Microhardness of non-stoichiometric $TiC_x$, plates prepared by chemical vapour deposition, J. Less Common Met. 163 (1990) 339–346.

[50] H.S. Kim, On the rule of mixtures for the hardness of particle reinforced composites, Mater. Sci. Eng. A 289 (2000) 30–33.

[51] M. Braem, V.E. Van Doren, P. Lambrechts, G. Vanherle, Determination of Young's modulus of dental composites: A phenomenological model, J. Mater. Sci. 22 (1987) 2037–2042.

**Figure captions**

Fig.1 SEM micrograph of the mixed powders of 90wt%Ti+10wt%C.

Fig.2 Schematic diagram showing set-up of high frequency induction cladding of Ti/graphite sample.

Fig.3 XRD pattern of (a) the raw Ti and graphite powders before cladding and (b) the composite coating.

Fig.4 XPS patterns of (a) Ti2p and (b) C1s of in-situ TiC/Ti composite coating.

Fig.5 Cross-sectional SEM images of (a) overview microstructure, (c) middle area, (b) upper area and (d) interface, of the in situ TiC/Ti composite coating.

Fig.6 Bright field TEM images of (a) spherical dispersed phase, (b) strip dispersed phase and (c) Ti matrix of the coating, and SAD patterns of (d) TiC, (e) α-Ti and (f) β-Ti phases thereon.

Fig.7 Microhardness profile of the in situ TiC/Ti composite coating (cross-section).

Fig.8 Indentation marks at a maximum depth of 1000 nm for (a) TiC phase, (b) α-Ti rich phase, (c) structure of β transformation on the composite coating and (d) Ti6Al4V substrate.

Fig.9 Nanoindentation results of (a) load-depth curve, (b) indentation hardness and (c) Young's modulus for different phases on the composite coating and the Ti6Al4V substrate (using a Poisson ratio of 0.25).

Fig.10 Cross-sectional SEM images of (a) overview microstructure, (b) magnified zone shown in square A, (c) magnified zone shown in square B and (d) magnified zone shown in square C, of the partly melted TiC/Ti composite coating under poor melting conditions (w = 10 kW, v = 1.2 mm/s, a = 4 mm).

Fig.11 Variation of Gibbs free energy and formation enthalpy of the reaction between Ti and graphite.

Fig.12 The calculated Ti–C phase diagram [44] (the arrow indicating the mole fraction of C is 0.3 in the raw powders used in the present work).

Fig.13 Rule of Mixtures results compared with measured value for TiC/Ti composite coating when assuming the matrix consists of (a) structure of β transformation, (b) equiaxed α-Ti phase, and (c) a mixture of 75vol% structure of β transformation and 25vol% equiaxed α-Ti phase.

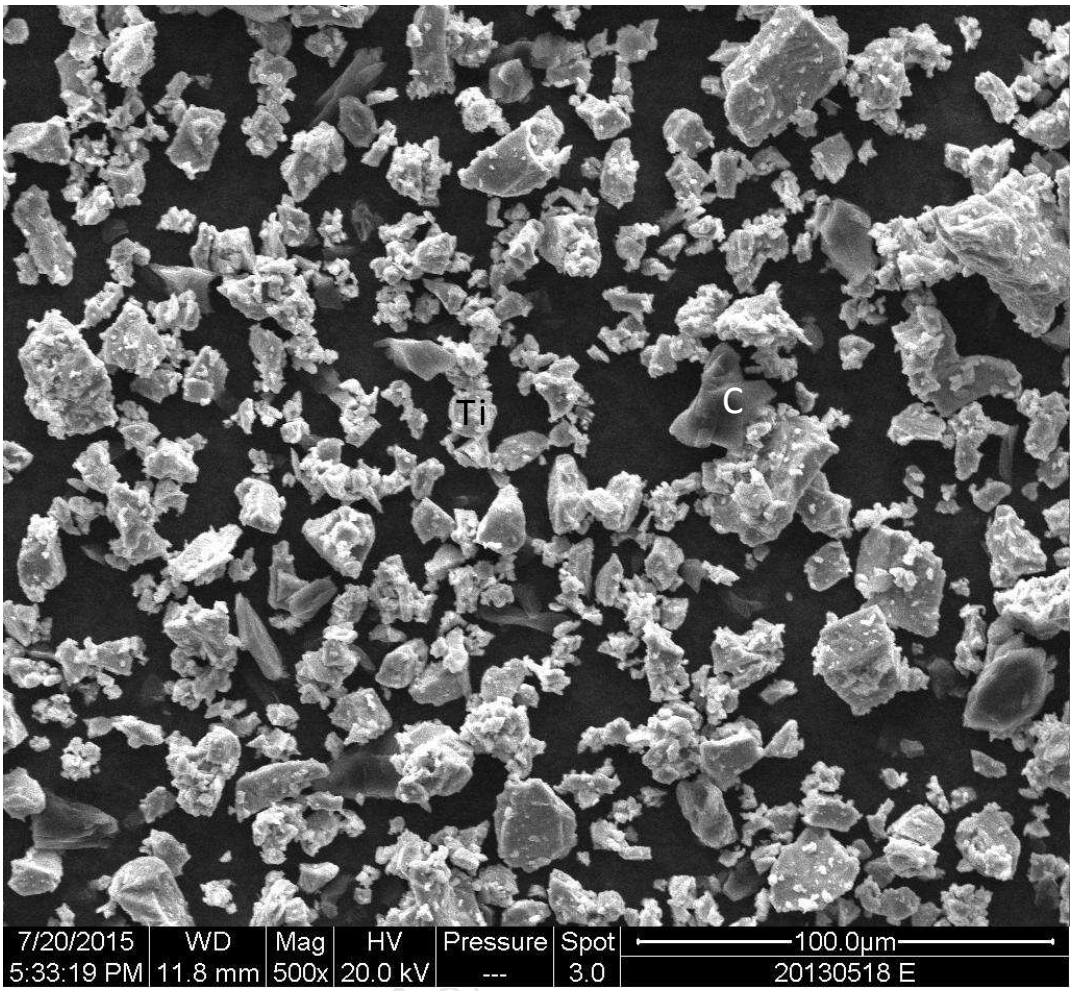
Ti
C
7/20/2015
5:33:19 PM
WD
11.8 mm
Mag
500x
HV
20.0 kV
Pressure
---
Spot
3.0
100.0µm
20130518 E

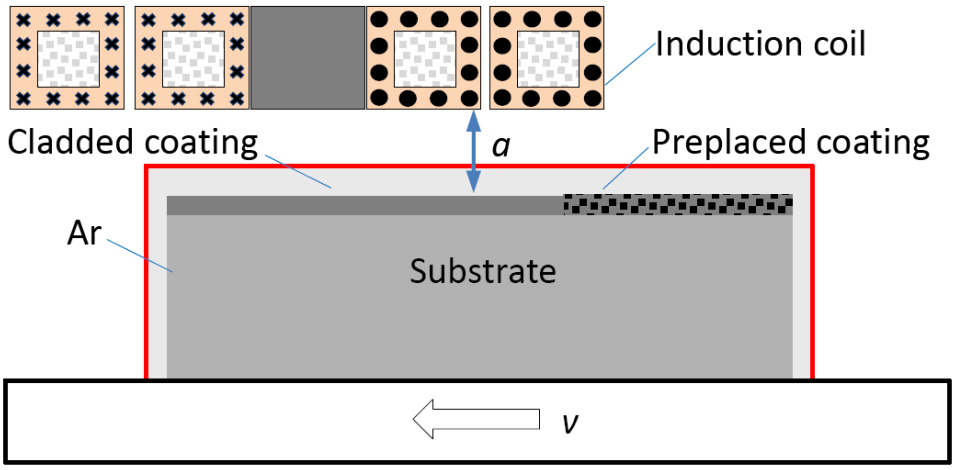

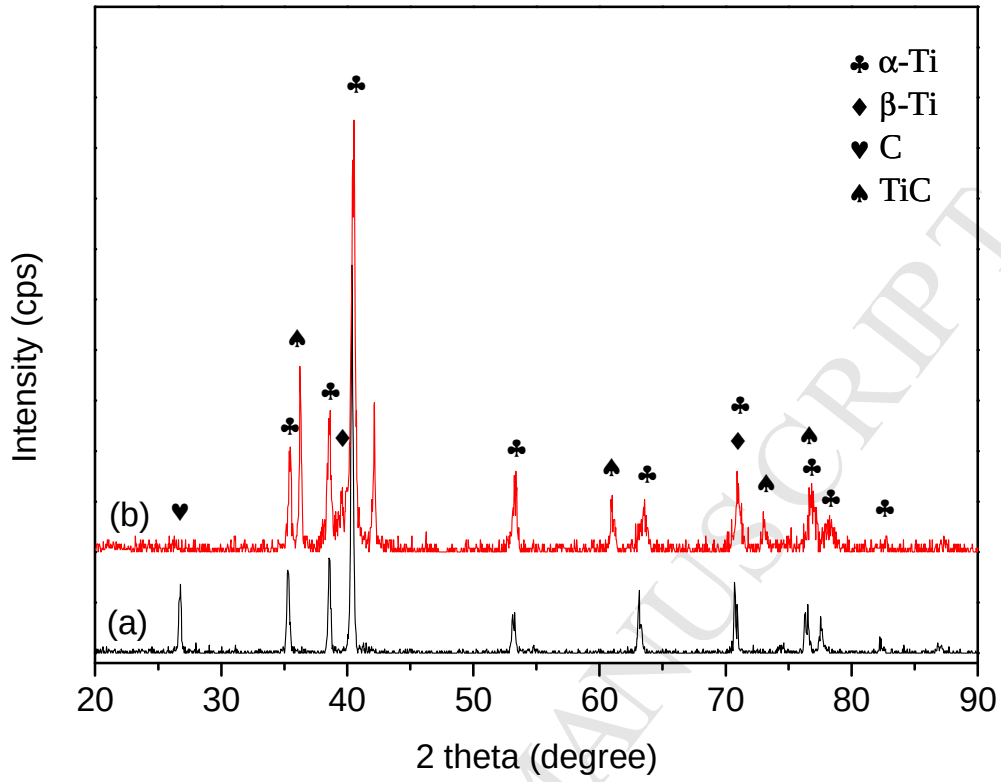

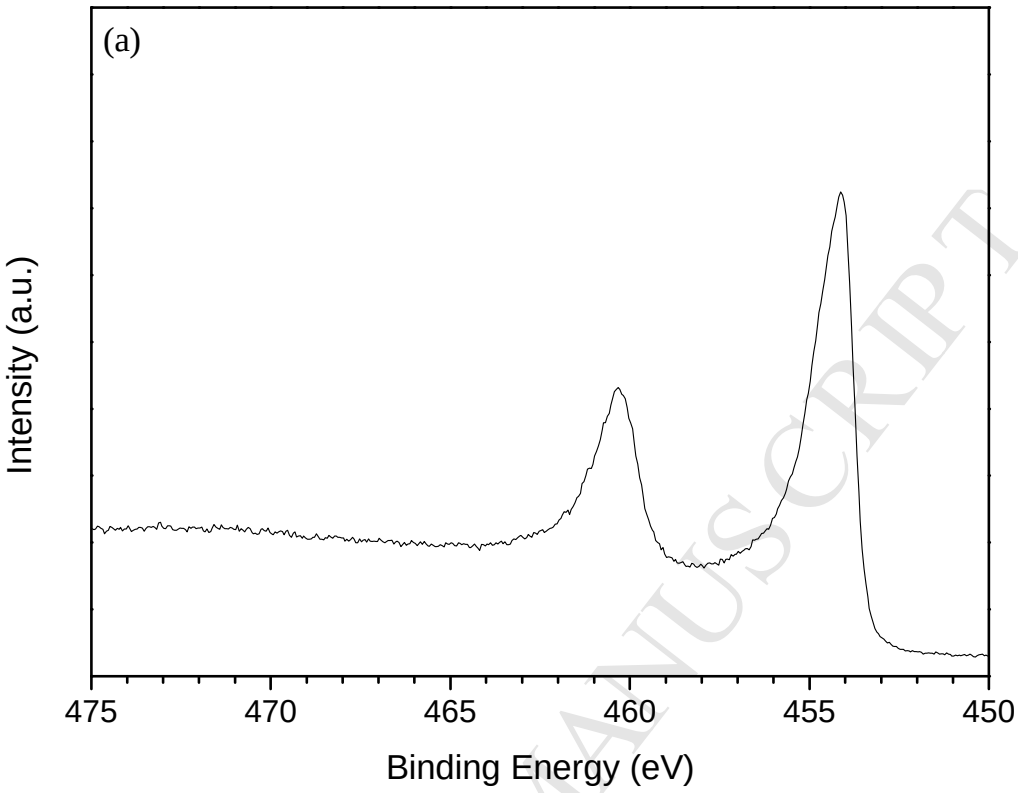

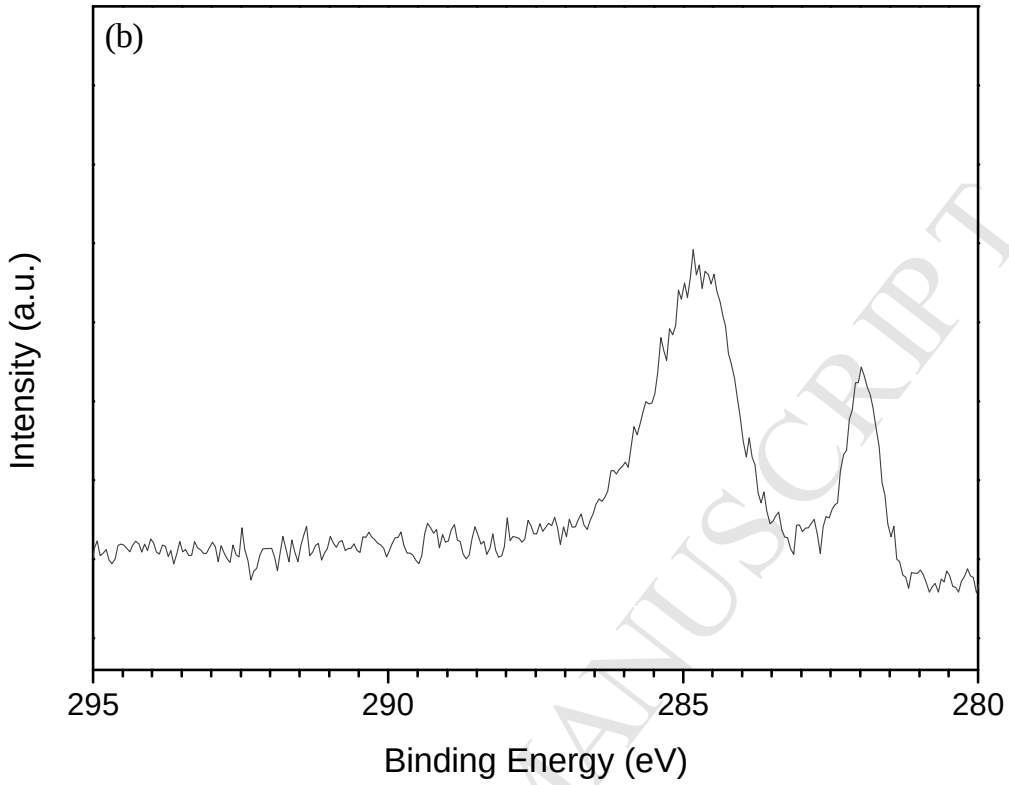

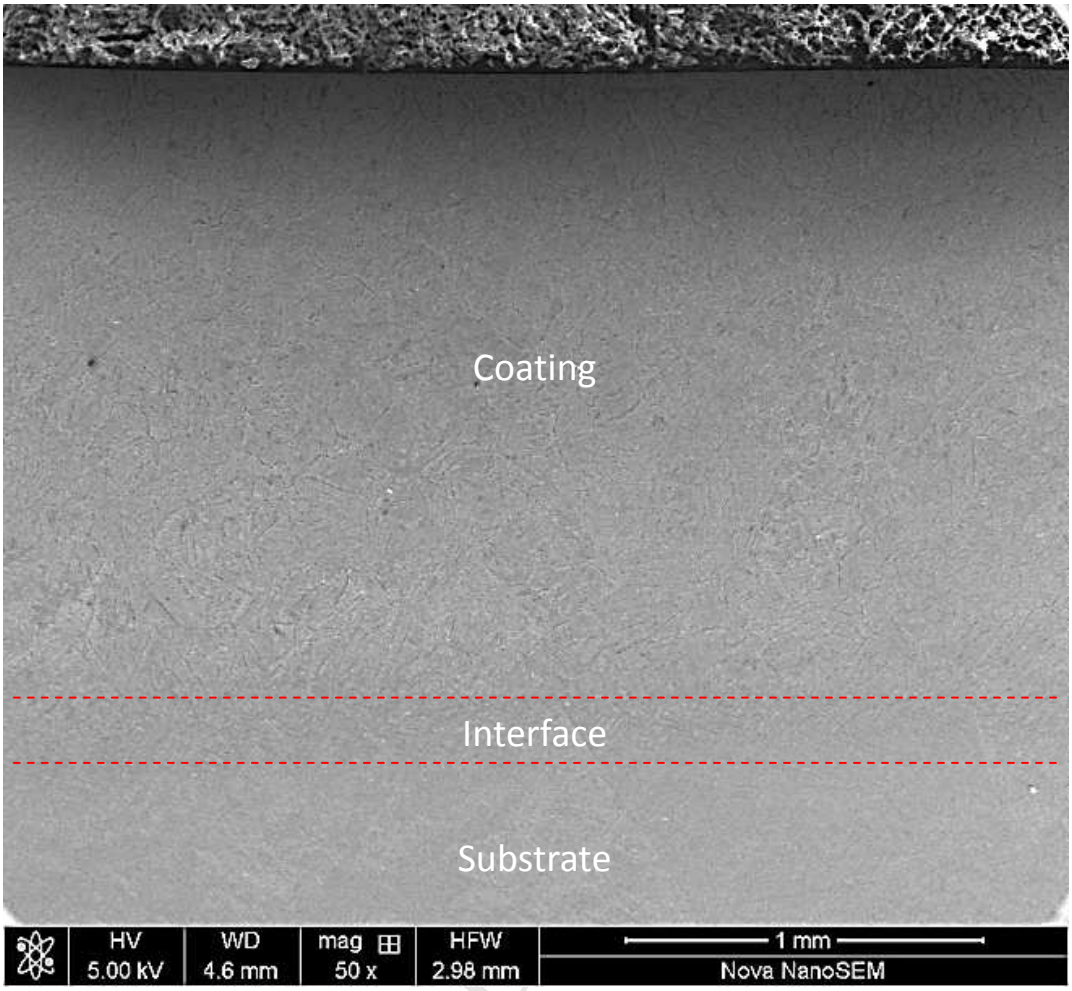

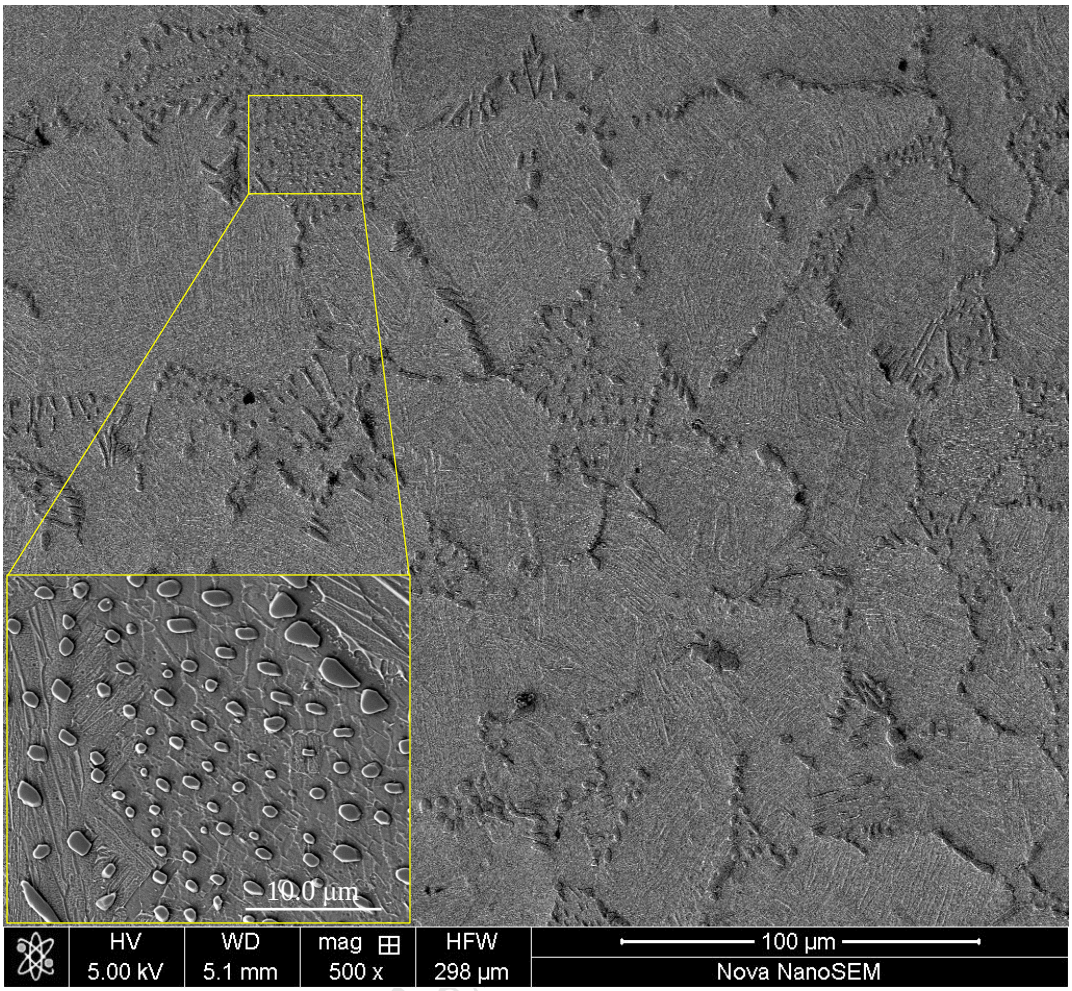

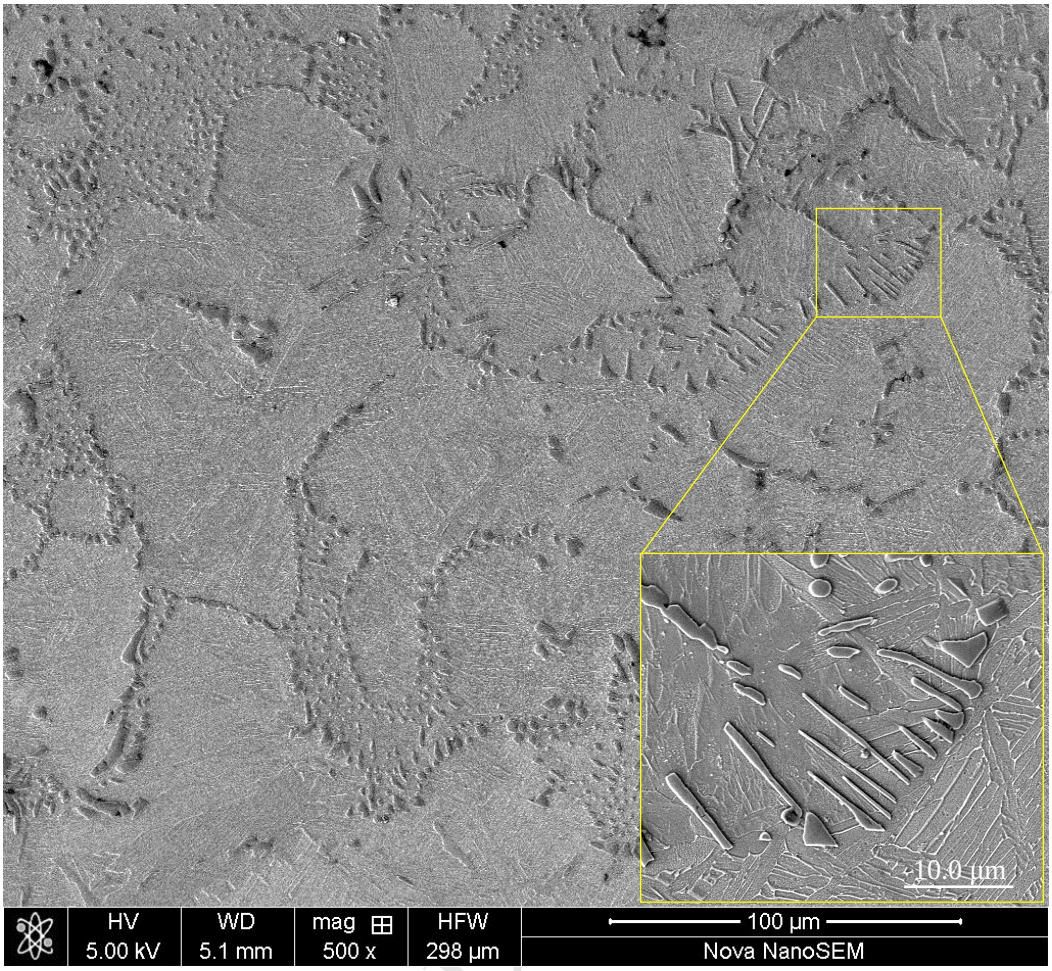

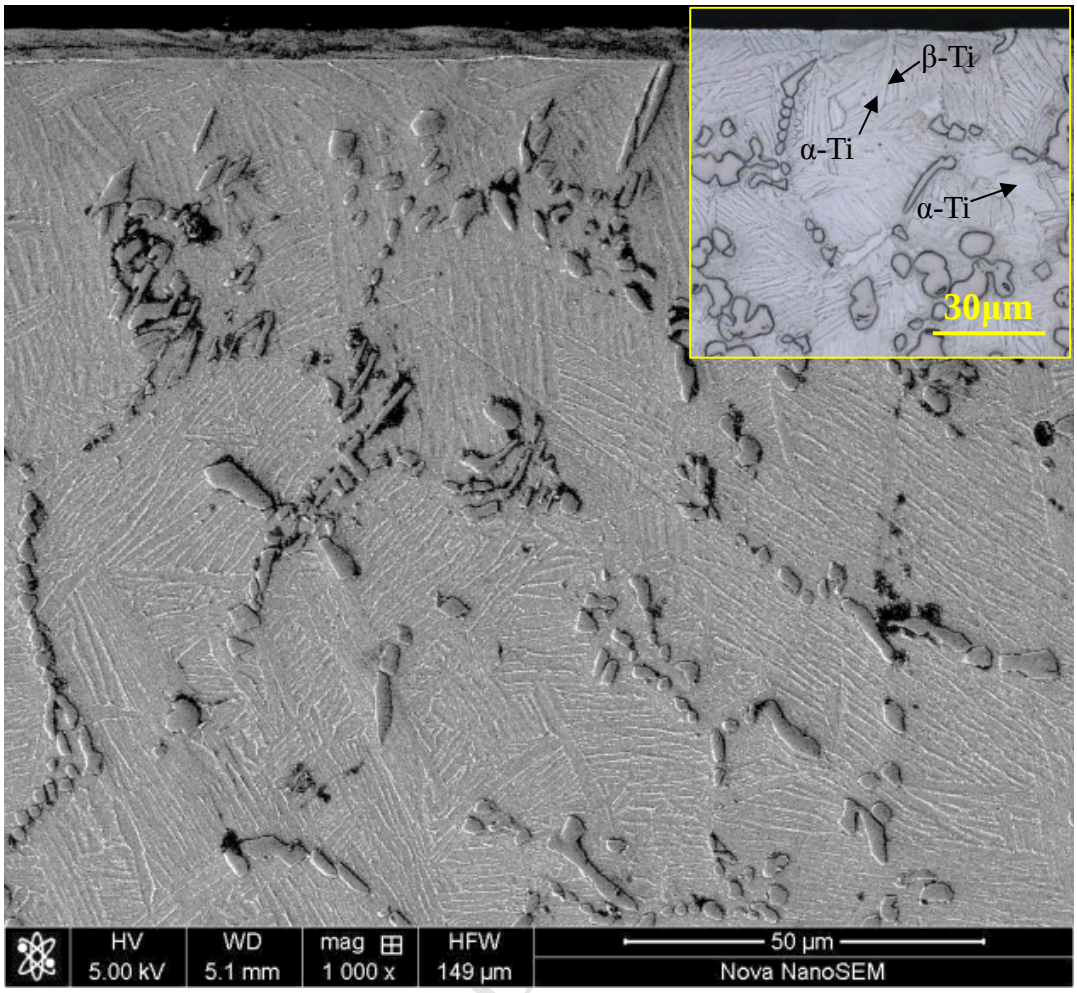

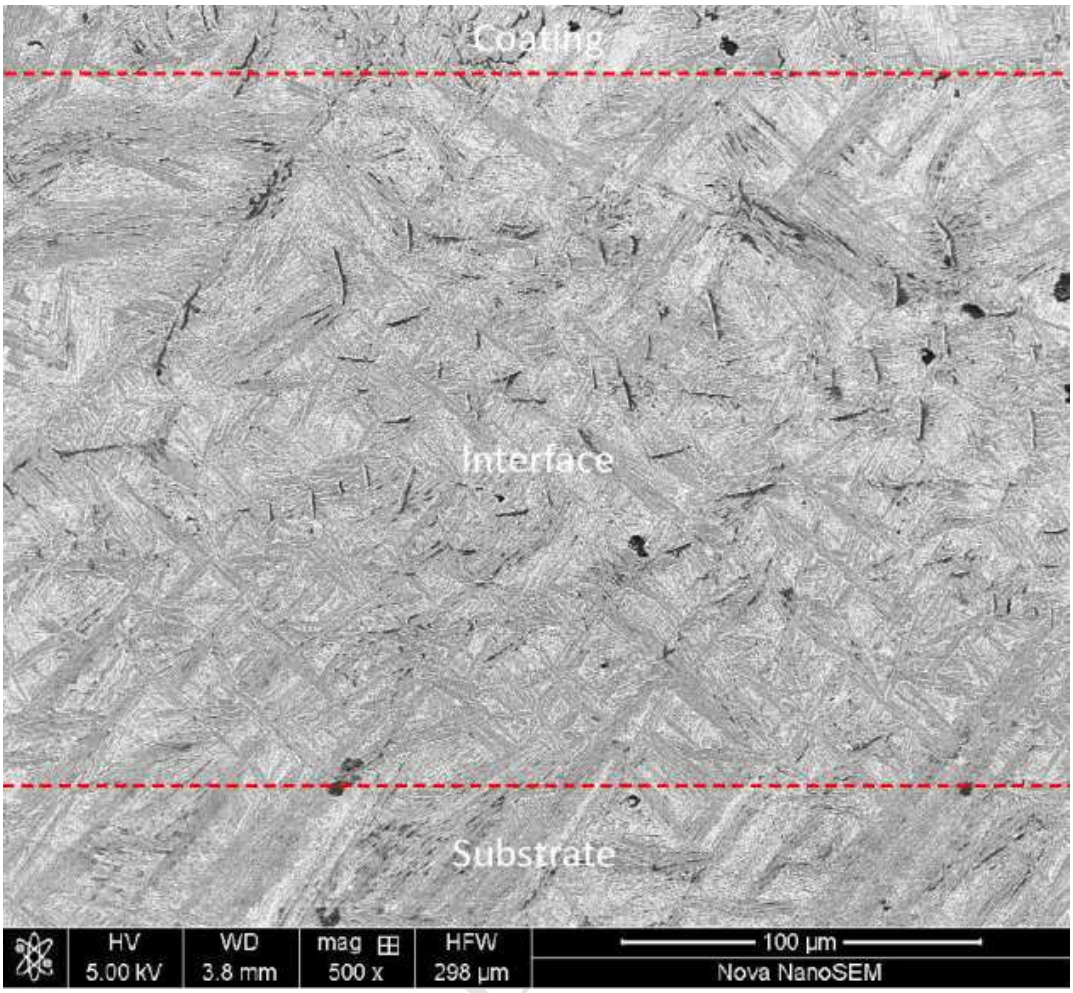
Coating
Interface
Substrate
HV
5.00 kV
WD
3.8 mm
mag
500 x
HFW
298 µm
100 µm
Nova NanoSEM

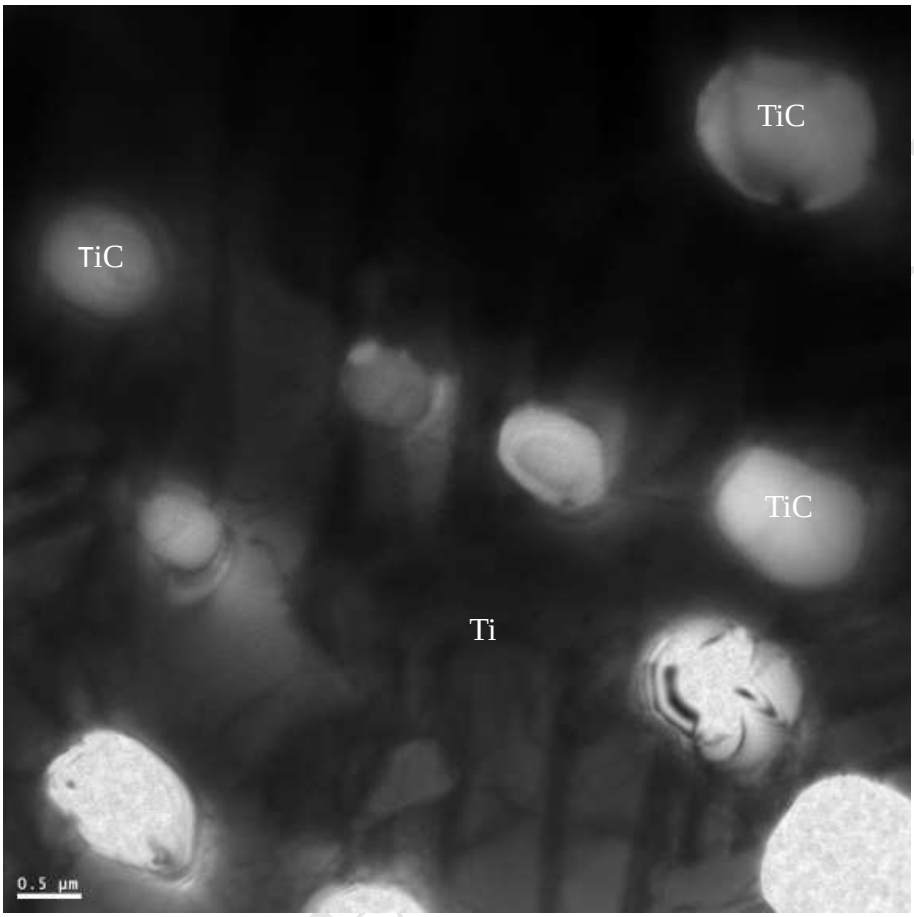

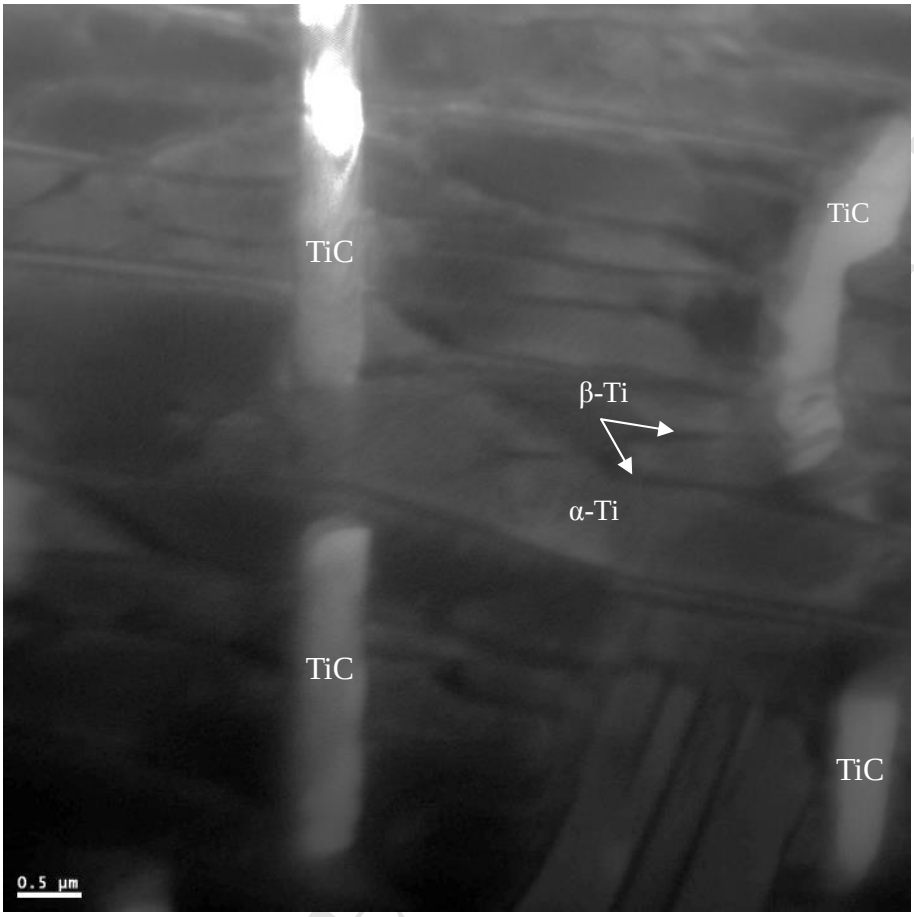

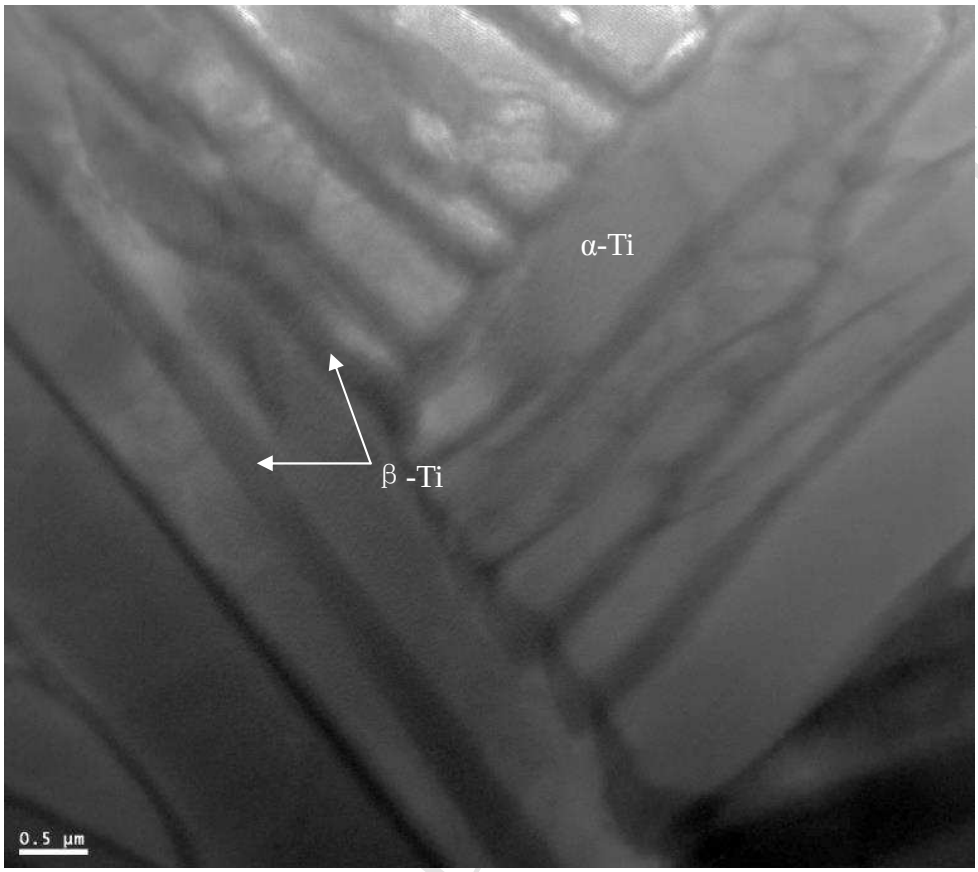

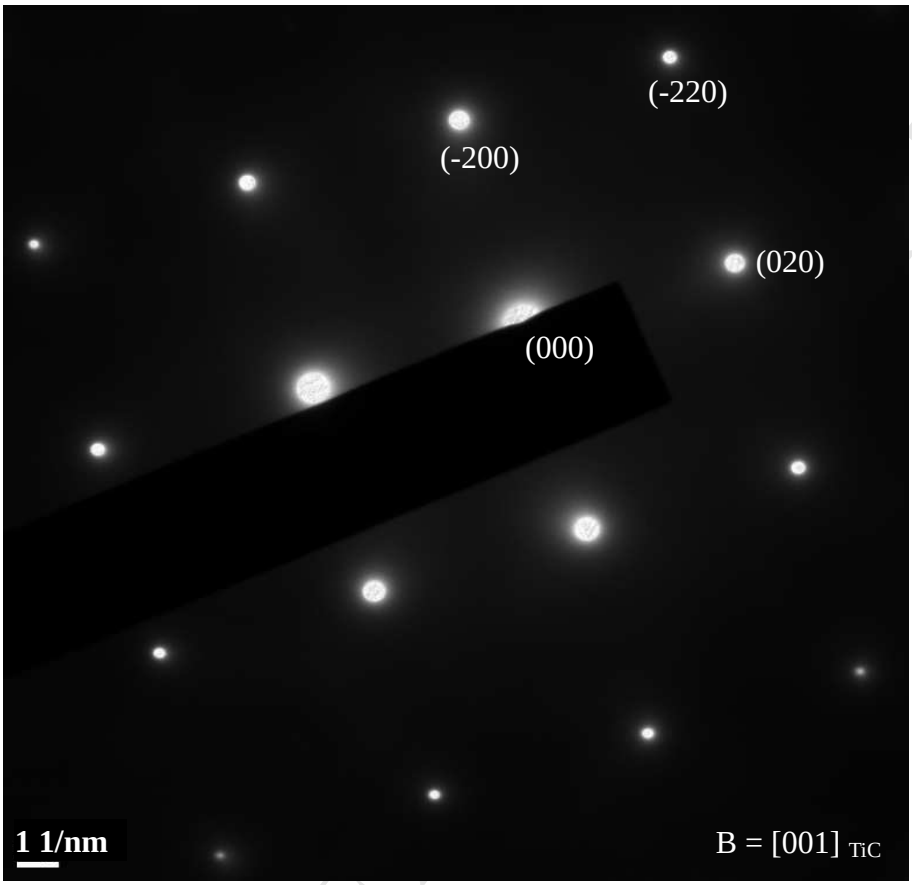

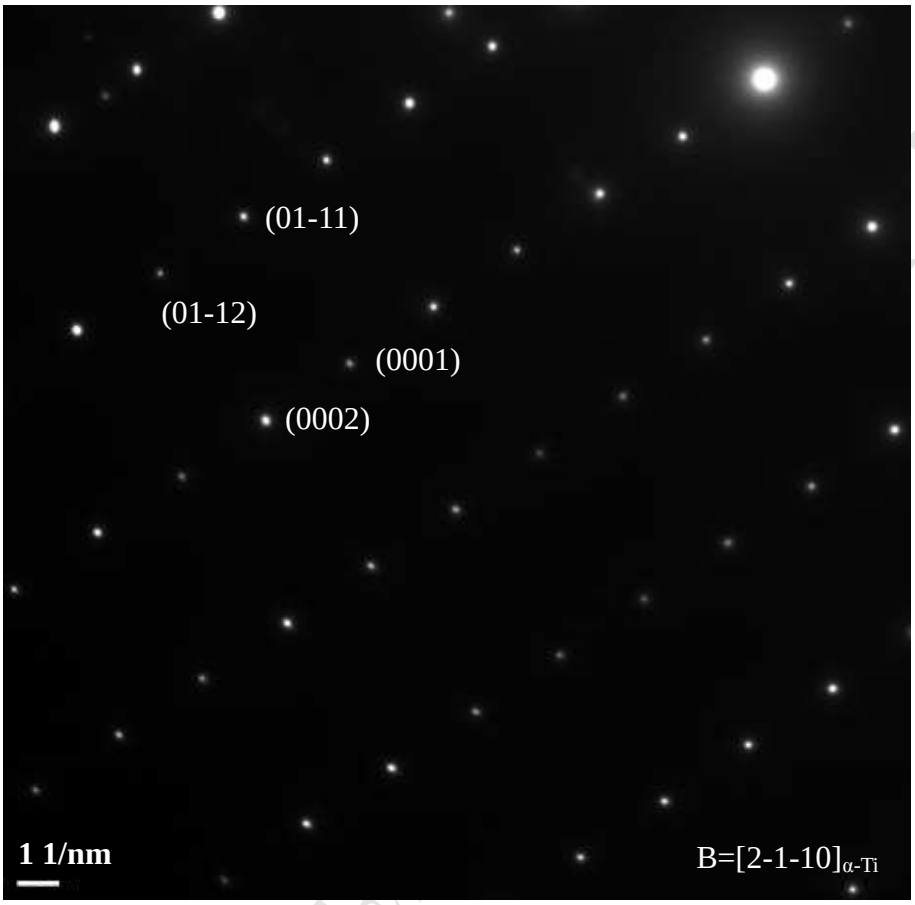

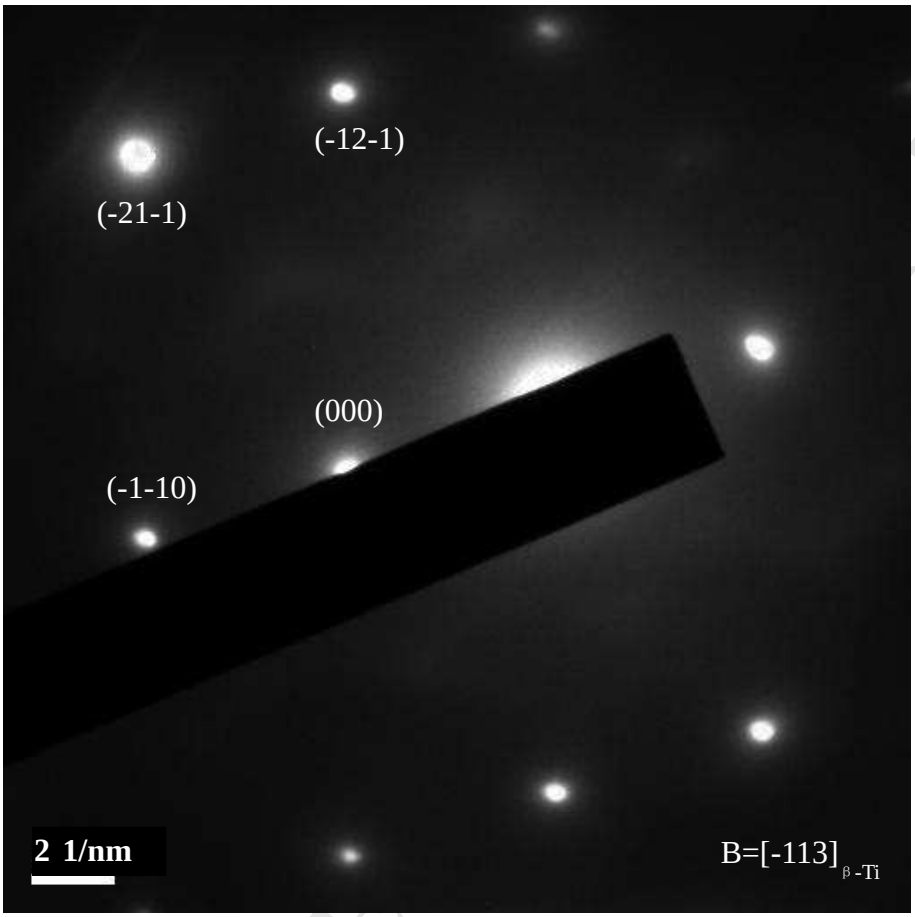

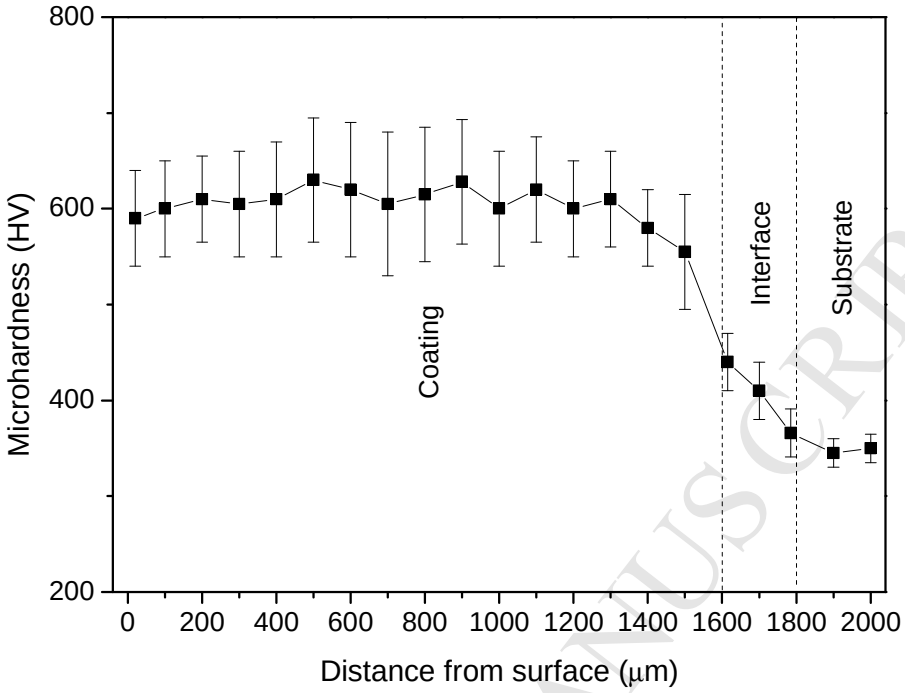

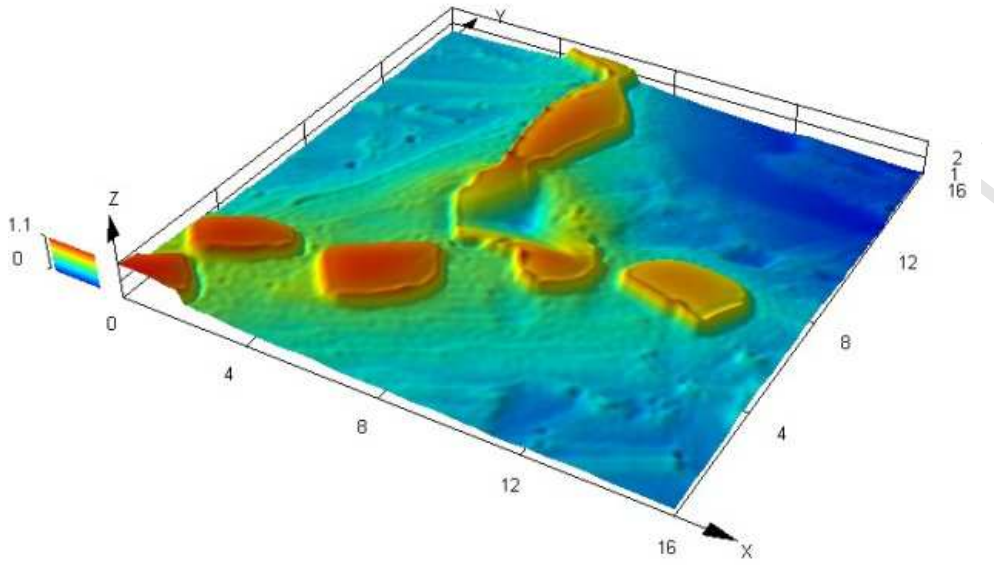

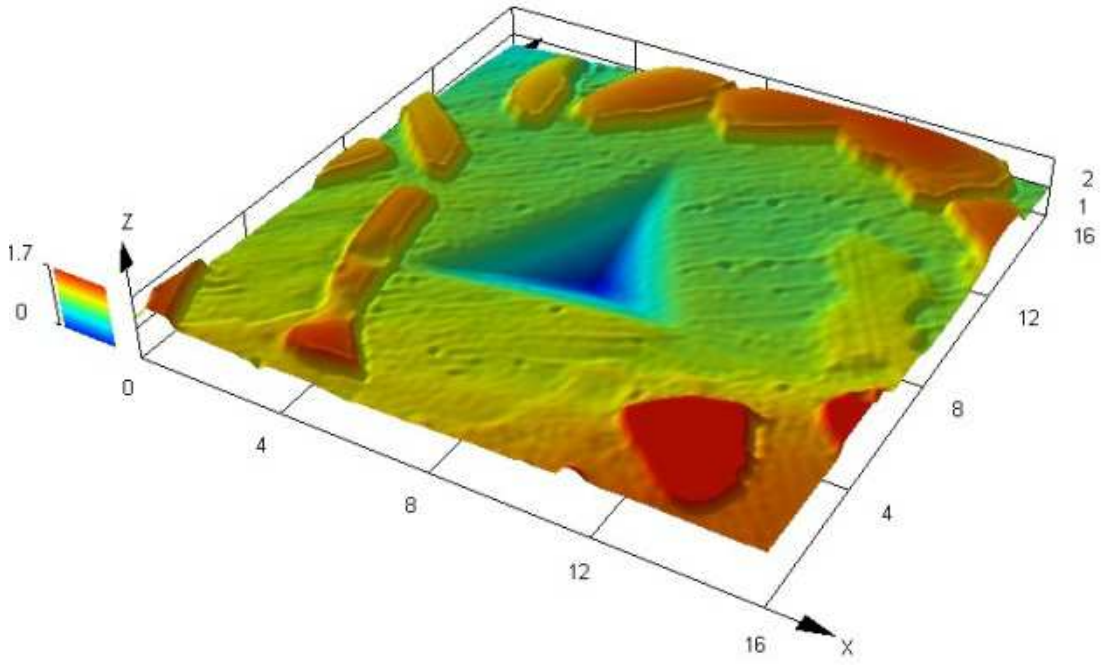

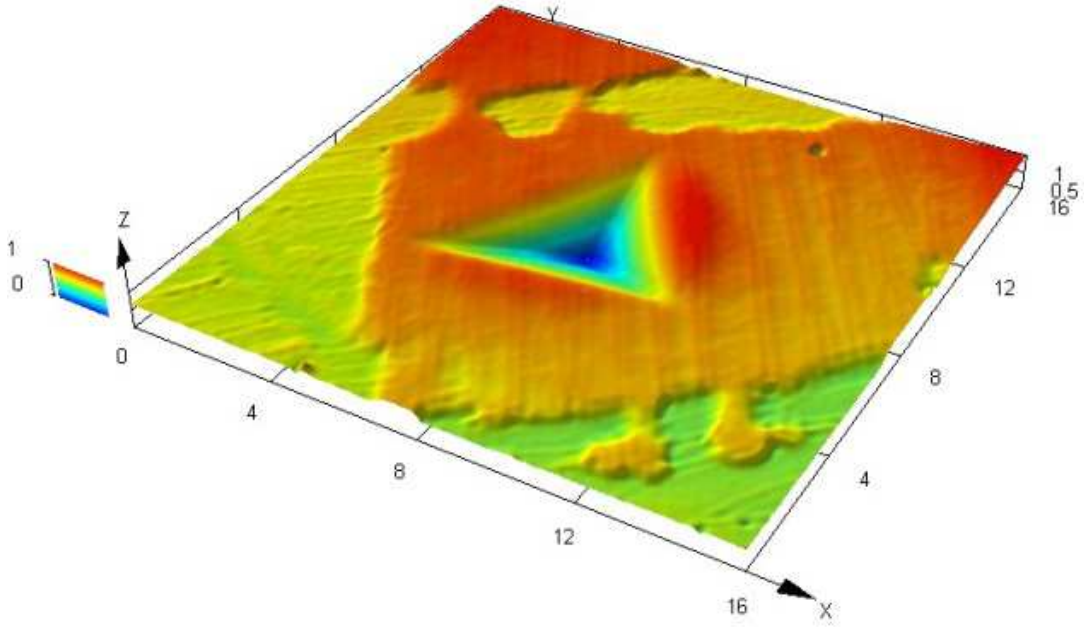

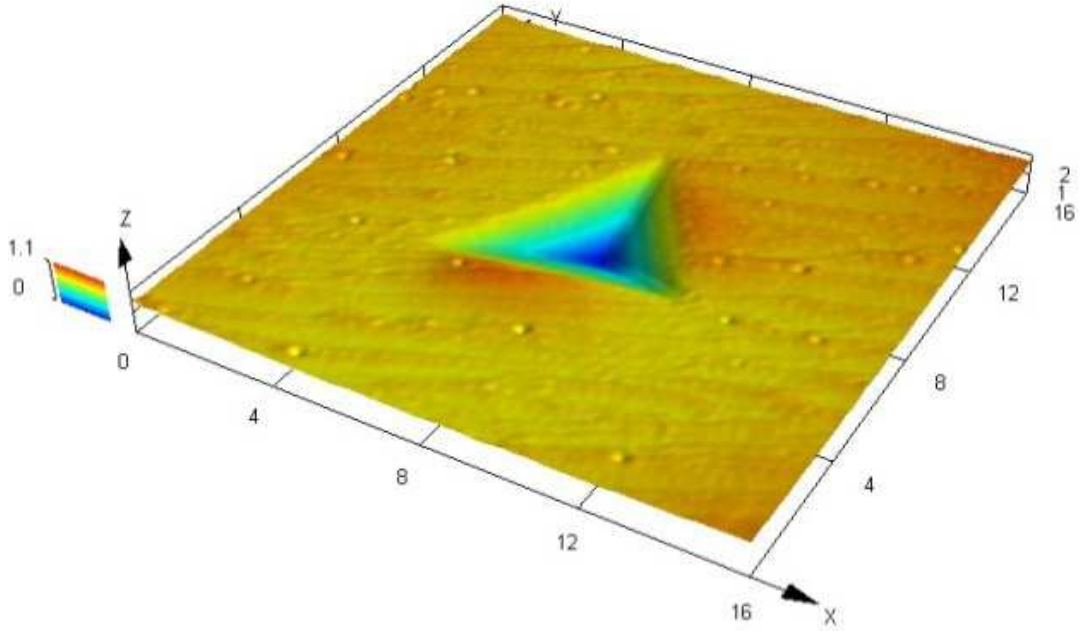

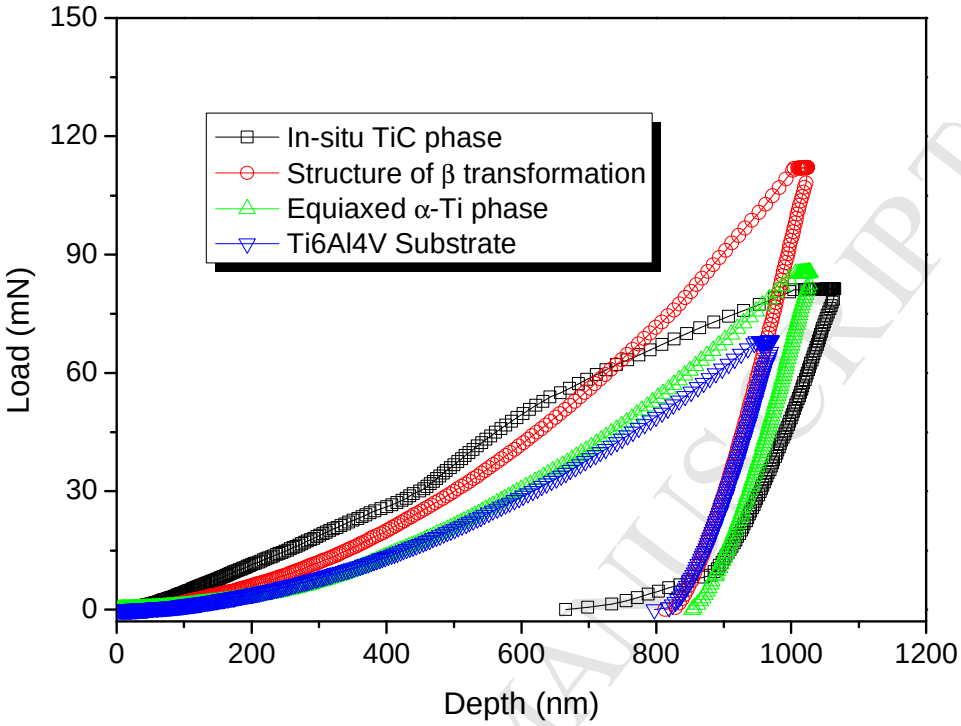

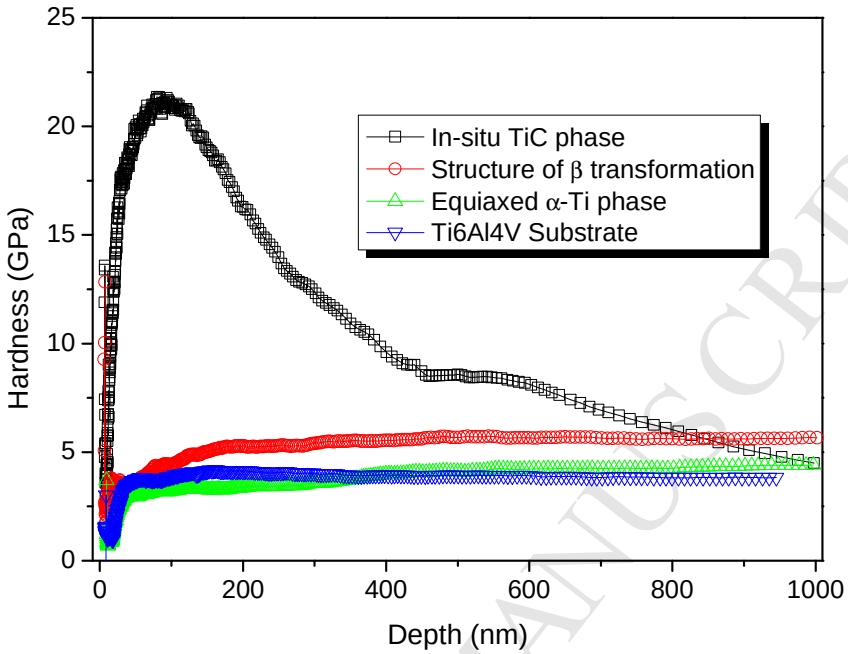

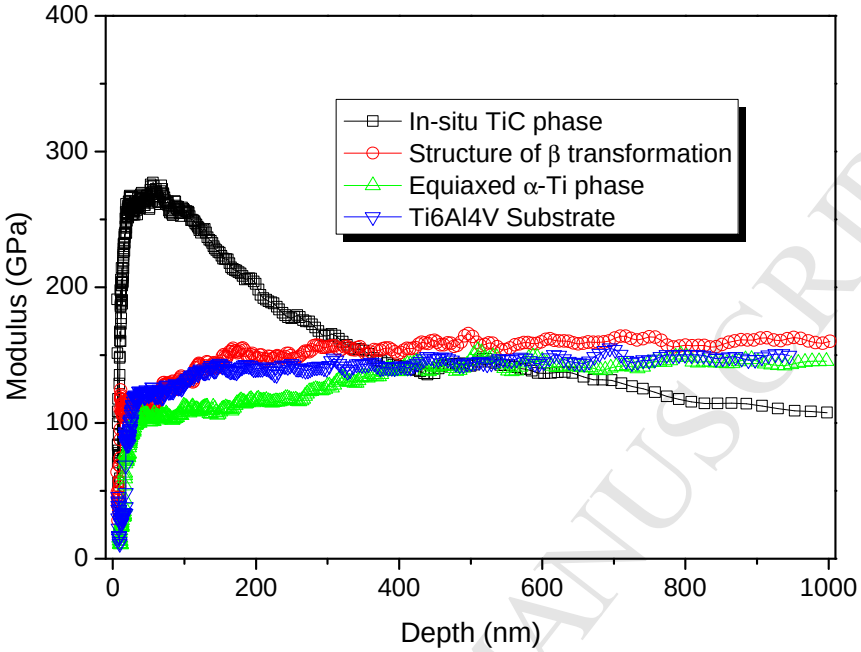

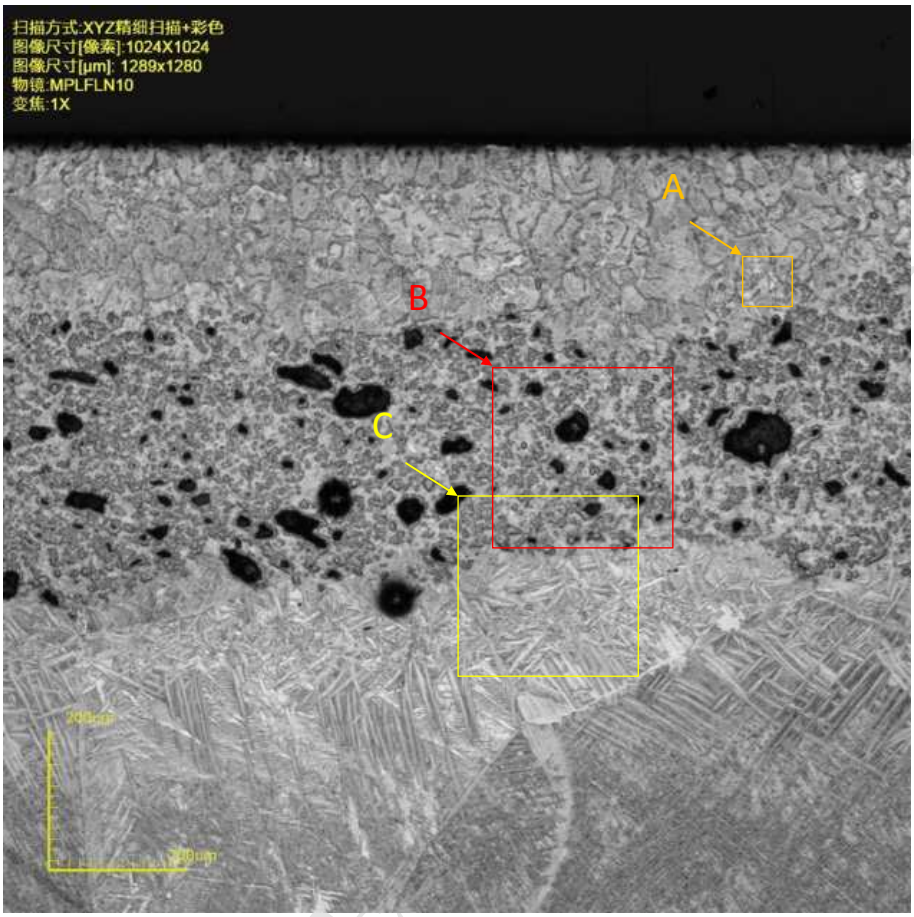

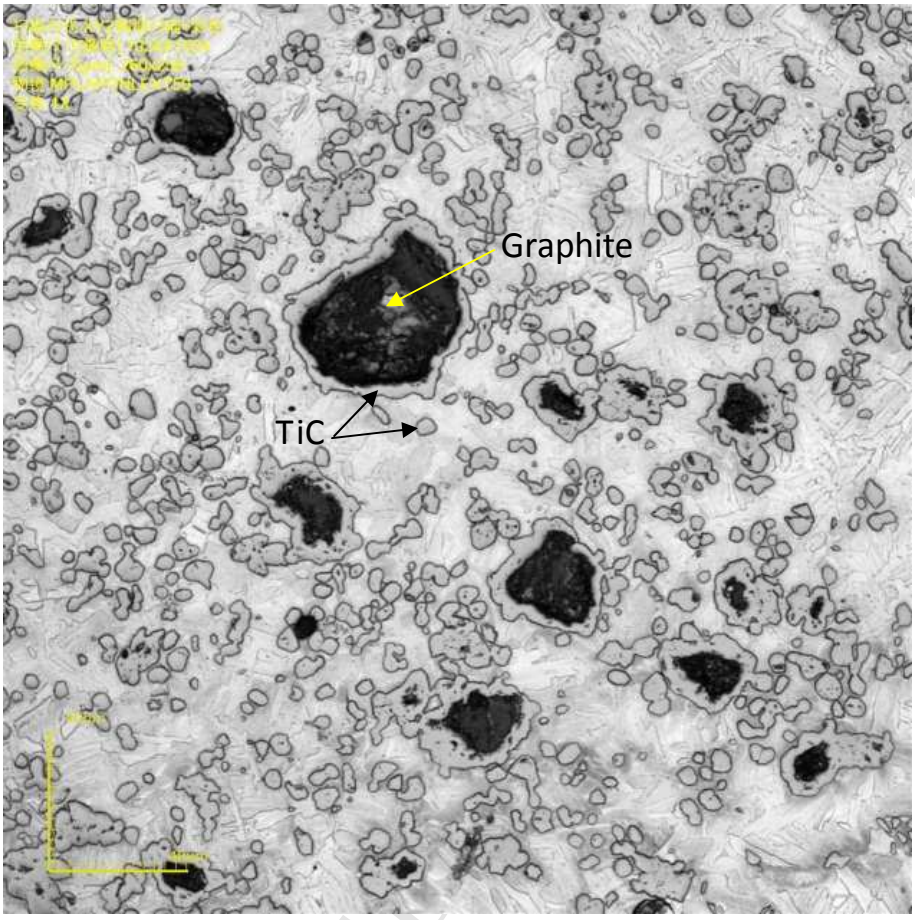

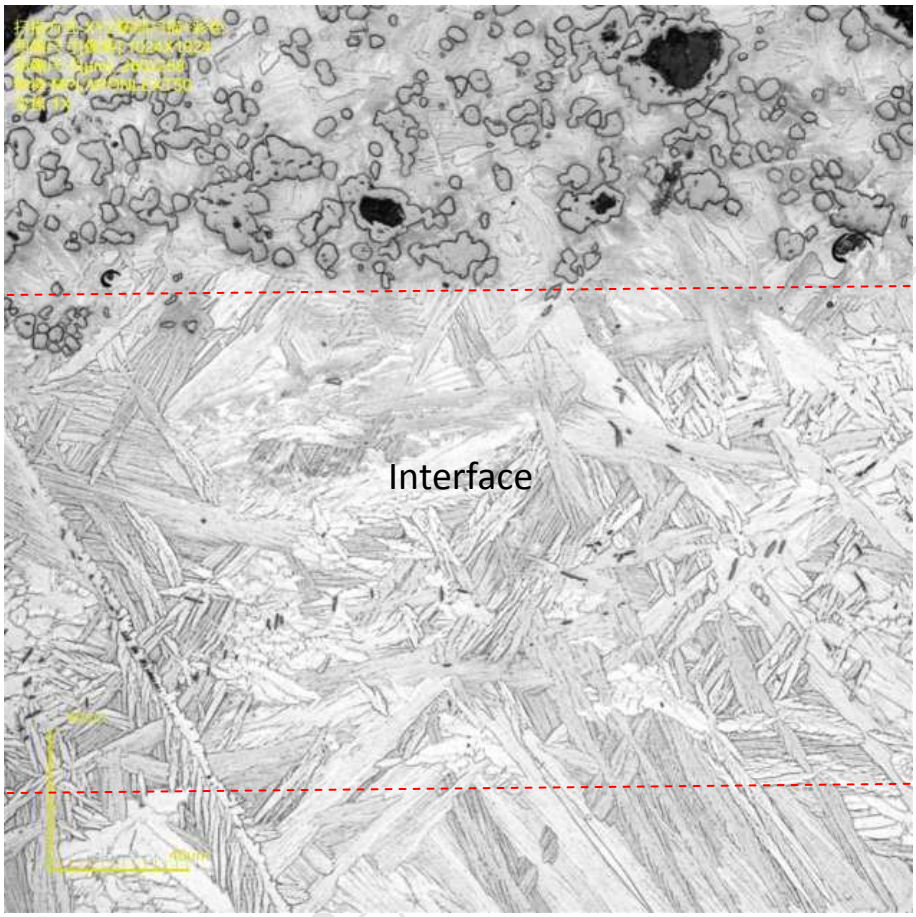

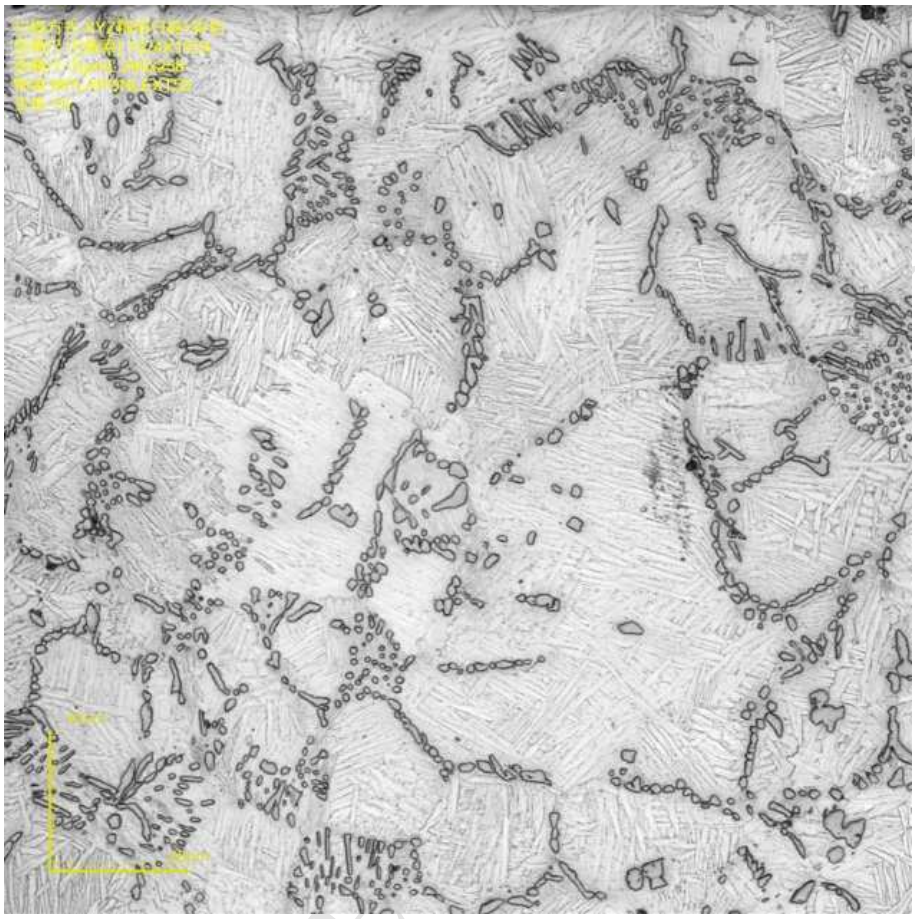

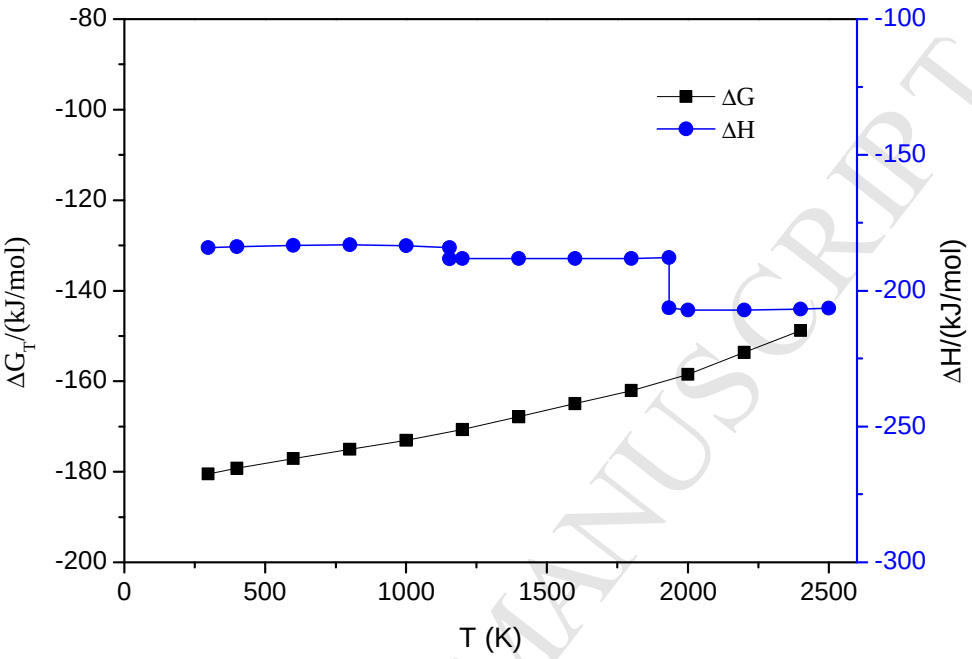

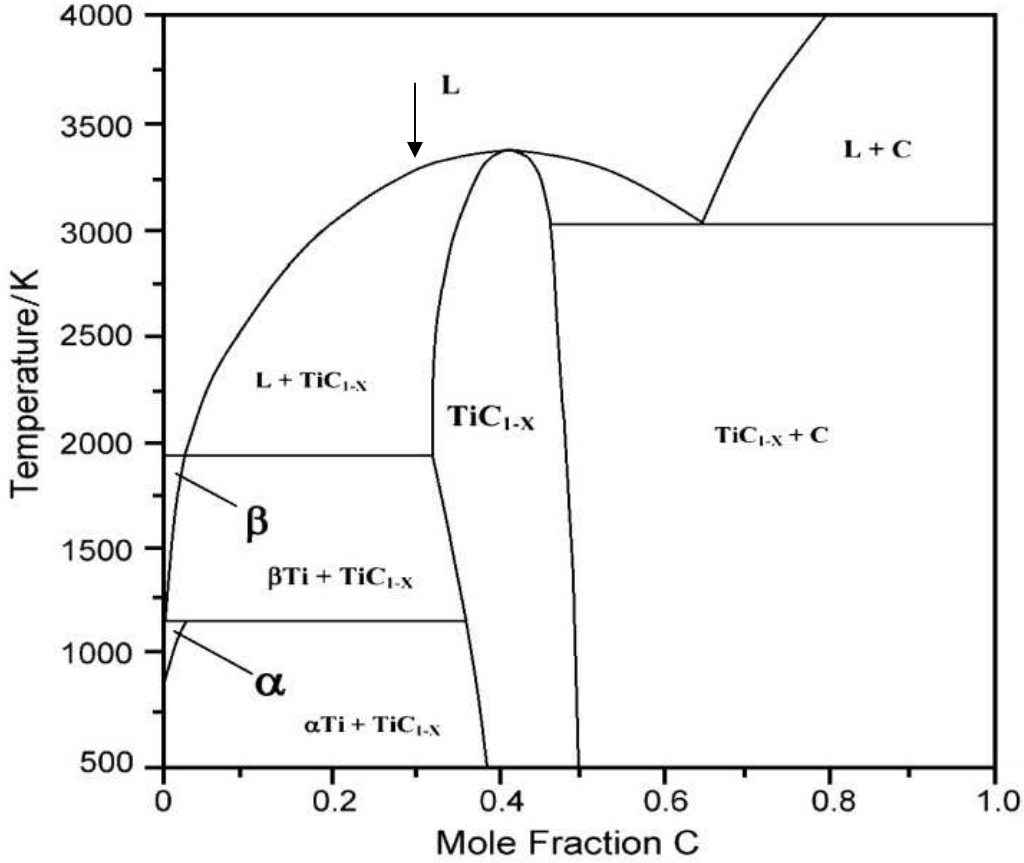

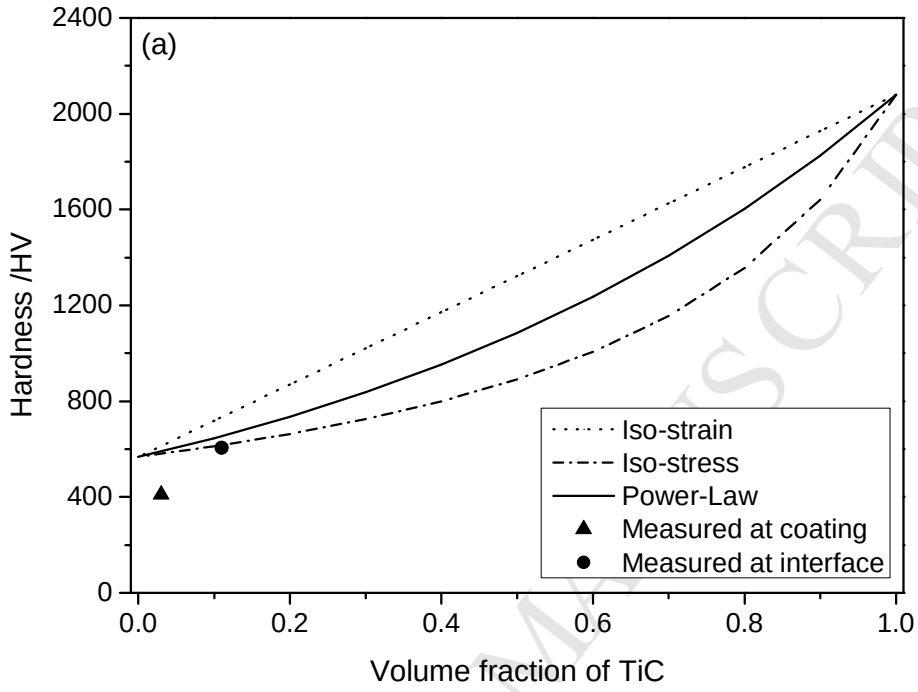

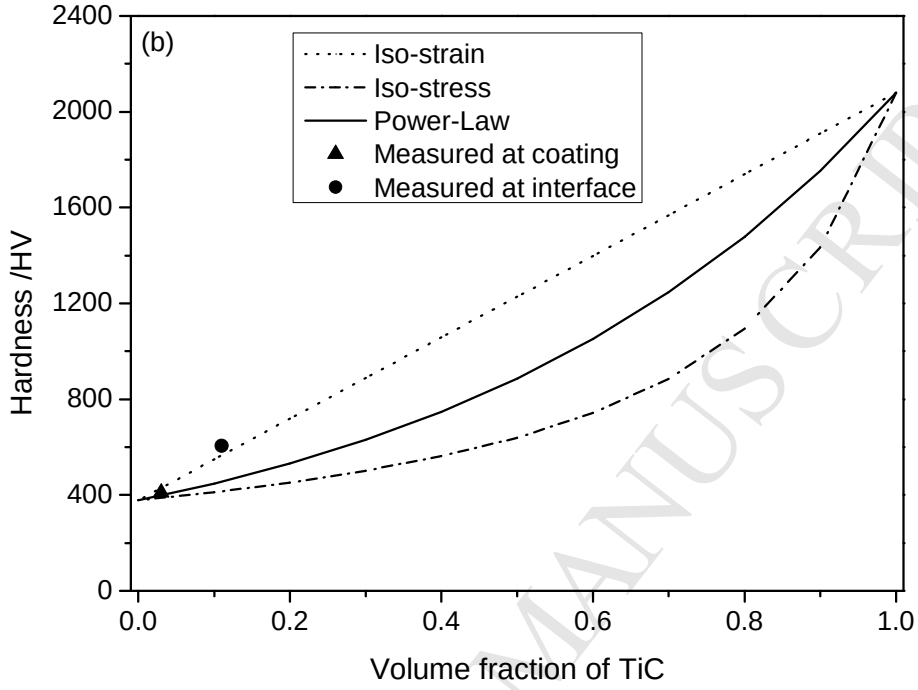

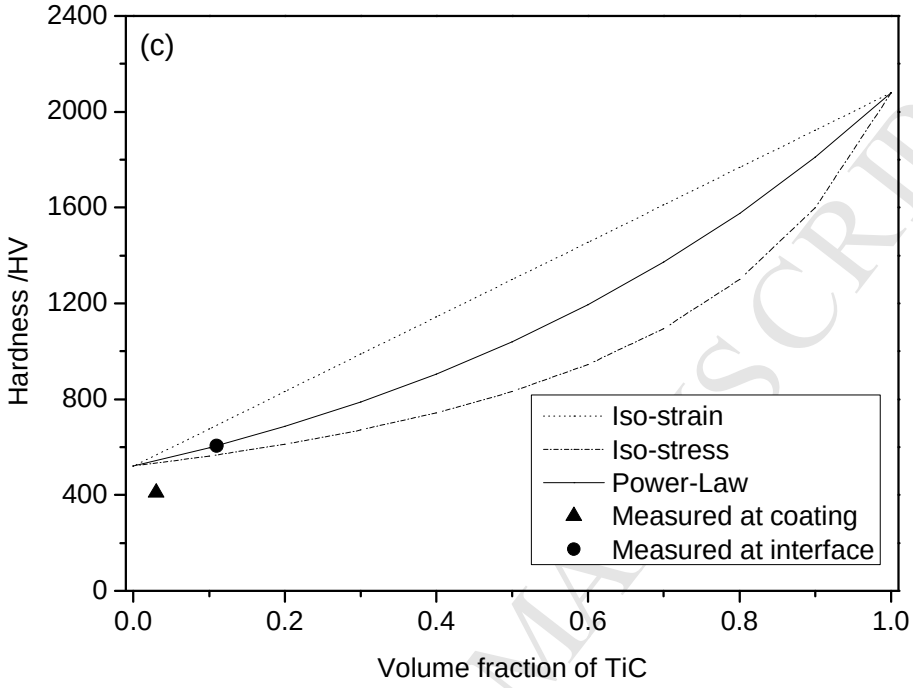

**Highlights**

- In situ synthesized TiC/Ti composite coating is achieved by induction cladding.
- The coating has smooth surface, dense structure, high hardness and good bond.
- Formation mechanisms of the coating and the in situ TiC particles are discussed.
- Nano/micro mechanical properties of different phases in the coating are studied.
- Hardness evolution of the in situ coating agrees well with the Rule of Mixtures.